TDP-43 toxic gain of function links ALS/FTLD-TDP and Alzheimer's Disease through splicing

Welmoed van Zuiden[1,2], Thea Meimoun[1,2], Chen Bar[1,2], Aviad Siany[1,2], Lihi Moshe[1,2], Nancy Yacovzada[1,2], Eviatar Weizman[3], Manuela Neumann[4,5], Aron S Buchman[6,7], Yanling Wang[6], David A Bennett[7], Jonathan D Glass[8], Adam N Trautwig[8], Nicholas T Seyfried[8], Johnathan Cooper-Knock[9], Eran Hornstein[1,2#]

[1]Department of Molecular Genetics, Weizmann Institute of Science, Rehovot, Israel

[2]Department of Molecular Neuroscience, Weizmann Institute of Science, Rehovot, Israel

[3]G-INCPM, Weizmann Institute of Science, Rehovot 7610001, Israel

[4]Department of Neuropathology, University of Tübingen, Tübingen, Germany

[5]Molecular Neuropathology of Neurodegenerative Diseases, German Center for Neurodegenerative Diseases, Tübingen, Germany

[6]Rush Alzheimer's Disease Center, Rush University Medical Center, Chicago, IL, USA

[7]Department of Neurological Sciences, Rush University Medical Center, Chicago, IL, USA

[8]Emory University School of Medicine, Atlanta, GA USA

[9]Sheffield Institute for Translational Neuroscience, University of Sheffield, Sheffield, S10 2HQ, UK

Corresponding Author: Eran.Hornstein@weizmann.ac.il

Abstract

Loss of nuclear TDP-43 splicing activity is a common feature across neurodegenerative diseases, but its relevance to Alzheimer's disease (AD) remains unclear. Here, we show that TDP-43 pathology in AD is broadly associated with splicing abnormalities, including aberrant splicing of amyloid precursor protein (APP). We demonstrate that TDP-43 drives the formation of elongated APP isoforms, APP751 and APP770. Thus, TDP-43 dysregulation disrupts APP695/751/770 alternative splicing across ALS/FTLD-TDP and AD, providing a compelling mechanism for a 37-year-old observation of APP isoform dysregulation. We further establish a mechanistic link between TDP-43 pathology, APP splicing, and Aβ pathology. Unexpectedly, this effect is mediated by a toxic gain of cytoplasmic TDP-43 function, rather than loss of its nuclear role. Using proximity proteomics and base editing in human iPSC-derived neurons, we show that TDP-43 pathology causes cytoplasmic co-sequestration of splicing regulators SCAF11, SRSF5, and TIAL1, which are involved in APP mis-splicing, but not in the regulation of other TDP-43 targets such as STMN2 or UNC13A. Together, our findings suggest that TDP-43-mediated splicing dysfunction upstream of APP contributes to the pathogenesis of seemingly disparate neurodegenerative diseases, uniting AD and ALS/FTLD-TDP through a shared molecular mechanism.

Introduction

TDP-43, that is encoded by the TARDBP gene, is a ubiquitous DNA- and RNA-binding protein that localizes to the nucleus, where it regulates RNA processing in many ways, including splicing [1,2]. In amyotrophic lateral sclerosis (ALS) and frontotemporal lobar degeneration (FTLD), TDP-43 forms insoluble cytoplasmic aggregates and is depleted from the nucleus, making it the most consistent pathological hallmark of ALS/FTLD-TDP [3,4]. In addition, TDP-43 pathology is found in up to 57% of Alzheimer's Disease (AD) cases, where it correlates with increased severity of symptoms [5,6]. TDP-43 pathology is associated with increased Tau burden [7], but the link between TDP-43 and amyloid-beta (Aβ) plaque formation is unclear and thus far only investigated in mice [8,9].

Dysregulation of alternative splicing has been broadly implicated in the pathogenesis of several neurodegenerative disorders, including ALS, FTD and AD [10,11]. TDP-43 is a principal splicing regulator and loss of TDP-43 from the nucleus disrupts splicing [12–15] . Consequently, cryptic exons are expressed in mRNAs such as cytoskeleton-related STMN2 and synaptic UNC13A [16–21]. Cryptic exon splicing of specific targets due to TDP-43 dysregulation is evident in several neurodegenerative states including ALS-FTLD, AD, and Huntington's disease [13,16,17,20,22–24]. However, TDP-43 regulates the splicing of hundreds of mRNAs and its impact on the transcriptome is broad [15,19,25,26]. While alternative splicing is known to play a role in AD [27–33], the contribution of TDP-43 pathology to this remains largely unexplored.

The proteolytic processing of amyloid precursor protein (APP) into the neurotoxic Aβ peptide is thought to be the crucial step in the development of Alzheimer's disease (AD) [34,35]. Aβ aggregation is associated with elevated activity of APP-cleaving enzymes [36,37] or to certain genetic variants in APP [38–40]. Intriguingly, alternative splicing of exons 7 and 8 governs the production of three major APP isoforms: the neuron-enriched APP695 and two other longer forms: APP751, and APP770. APP751 and APP770 contain the Kunitz protease inhibitor (KPI) domain while APP770 additionally includes the OX-2 domain [41,42]. Protein and mRNA levels of KPI(+)APP are elevated in AD and have been associated with increased Aβ production [43–47]. However, the mechanistic underpinning of alternative splicing of APP in AD is not well understood.

Here, we show that TDP-43 pathology is broadly associated with splicing abnormalities in AD including the regulation of APP alternative splicing. This finding extends across neurodegenerative diseases,

suggesting a commonality for ALS/FTLD-TDP and AD. Moreover, this analysis reveals the mechanistic underpinning of APP isoform dysregulation that was originally reported several decades ago. In addition, we demonstrate a link between TDP-43 pathology, APP splicing and Aβ pathology. Surprisingly, toxic gain of TDP-43 function, not loss of nuclear TDP-43 function, causes this shift in APP isoforms. We characterize the mechanism which involves cytoplasmic co-sequestration of three other splicing regulators from the nucleus: SCAF11, SRSF5 and TIAL1. Taken together, TDP-43 pathology ties seemingly disparate neurodegenerative diseases together via splicing dysfunction.

Results

TDP-43 pathology is associated to splicing abnormalities in Alzheimer's Disease

To investigate whether TDP-43 pathology contributes to alternative splicing in AD, we analyzed RNA sequencing data of post-mortem dorsolateral prefrontal cortex (DLPFC) tissue samples from the Religious Orders Study and Rush Memory and Aging Project (ROSMAP [48], Synapse: syn4164376 [49]). We performed splicing analysis with MAJIQ [50], comparing patients clinically diagnosed with AD dementia (N = 253) to controls without cognitive impairment (N = 201), and comparing brain tissues with TDP-43 pathology (N = 150) to those without (N = 150) (**Supplementary Table 1**). In total, aberrant splicing events were found in 2890 genes in AD cases compared to control, and in 1596 genes in samples with TDP-43 pathology (|deltaPSI| > 0.02, signifying the change in percent spliced in (PSI) between conditions, and P-value < 0.05; **Supplementary Table 2**). A significant portion of the genes alternatively spliced in AD was also alternatively spliced upon TDP-43 pathology (Fisher's Exact P-value < 0.0001, **Figure 1A**). This includes the majority of genes previously reported to be mis-spliced in AD by Raj et al. [27]. Moreover, the exact splice junctions alternatively used in AD significantly overlapped with those alternatively used upon TDP-43 pathology (Fisher's Exact P-value < 0.0001, **Figure 1B**). Notably, the magnitude and direction of splicing changes at these overlapping junctions were remarkably concordant (Pearson r = 0.934, P < 0.0001, **Figure 1C**), strongly implicating TDP-43 pathology as a major driver of splicing dysregulation in AD.

Among the genes mis-spliced in AD and upon TDP-43 pathology is PICALM, which is genetically associated to AD [51] and was previously reported to be mis-spliced in AD [27]. Usage of the splice junction between exons 12 and 14 was increased by 8% in AD (P-value < 0.001) and by 6% upon TDP-43 pathology (P-value < 0.01, **Figure 1D**). Accordingly, the splice junction between exons 13 and 14 was used 9% less in AD (P-value < 0.001) and 6% less upon TDP-43 pathology (P-value < 0.05, **Figure 1D**). Other highly mis-spliced targets include NCAM1 (**Supplementary Figure 1A**) and KIDINS220 (**Supplementary Figure 1B**), both of which have been implicated in AD [52–54].

We next asked whether TDP-43 pathology could contribute to aberrant splicing in the microtubule-associated protein Tau (MAPT) gene. More than 30 isoforms are predicted to arise as a result of alternative splicing of MAPT mRNA, but most variation comes from altered inclusion of exons 2, 3 and 10 [55]. Analysis of ROSMAP data revealed an increase in the usage of the junction between exons 2

and 5 in AD and upon TDP-43 pathology, and a concomitant decrease in the inclusion of exon 3 (5%, P-value < 0.05, **Figure 1E**). Thus, TDP-43 pathology broadly affects splicing of key effectors of AD.

Amyloid precursor protein is aberrantly spliced upon TDP-43 pathology

Alternative splicing of amyloid precursor protein (APP) has been recognized in AD for more than three decades [43–46,56,57], however, its mechanistic underpinnings remain unknown. We reveal that APP mRNA is significantly mis-spliced both in AD and upon TDP-43 pathology (MAJIQ P-value < 0.0001, **Figure 1F, G**). Splicing analysis revealed a 5% fewer splice events resulting in APP695 in samples with TDP-43 pathology compared to those without (P-value < 0.01), and reciprocally exon 7 or exons 7-and-8 inclusion, leading to APP751 or APP770 formation, were increased by 5% (P-value < 0.01, **Figure 1G** and **Supplementary Table 3**).

An orthogonal bioinformatic approach, with RNA-Seq by Expectation Maximization RSEM [58] (N=505) found a 20% lower expression of APP695 (P-value < 0.001) but higher APP751+APP770 (P-value < 0.01) in samples with TDP-43 pathology, relative to those without (**Figure 1H**).

To verify the association of TDP-43 pathology to APP splicing, we analyzed RNA sequencing data from neuronal nuclei displaying TDP-43 pathology in ALS/FTLD-TDP human brains [26] (**Figure 1I**). Splicing analysis comparing TDP-43-positive to TDP-43-depleted nuclei revealed 8837 aberrant splicing events (|deltaPSI| > 0.1 and P-value < 0.1) in 2947 genes, including UNC13A and STMN2 (**Supplementary Table 2**). Genes alternatively spliced upon TDP-43 pathology in ALS/FTLD-TDP tissues significantly overlapped with those mis-spliced upon TDP-43 pathology in AD tissues (Fisher's Exact P-value < 0.0001, **Supplementary Figure 1C**). In TDP-43-depleted nuclei, usage of the splice junction between APP exons 6 and 9 (leading to the generation of isoform APP695, **Figure 1F**) was decreased by 10%, compared to control nuclei (P-value < 0.0001, **Figure 1J** and **Supplementary Table 3**). This was accompanied by a 10% increase in the production of APP751 (P-value < 0.0001, **Figure 1J**), which is a 1.3-fold change relative to TDP-43-positive nuclei. These results, arising from direct comparison between pure TDP-positive and -negative populations, confirm APP mis-splicing downstream of TDP-43 pathology and extend the observations to ALS/FTLD-TDP, suggesting a molecular commonality across neurodegeneration.

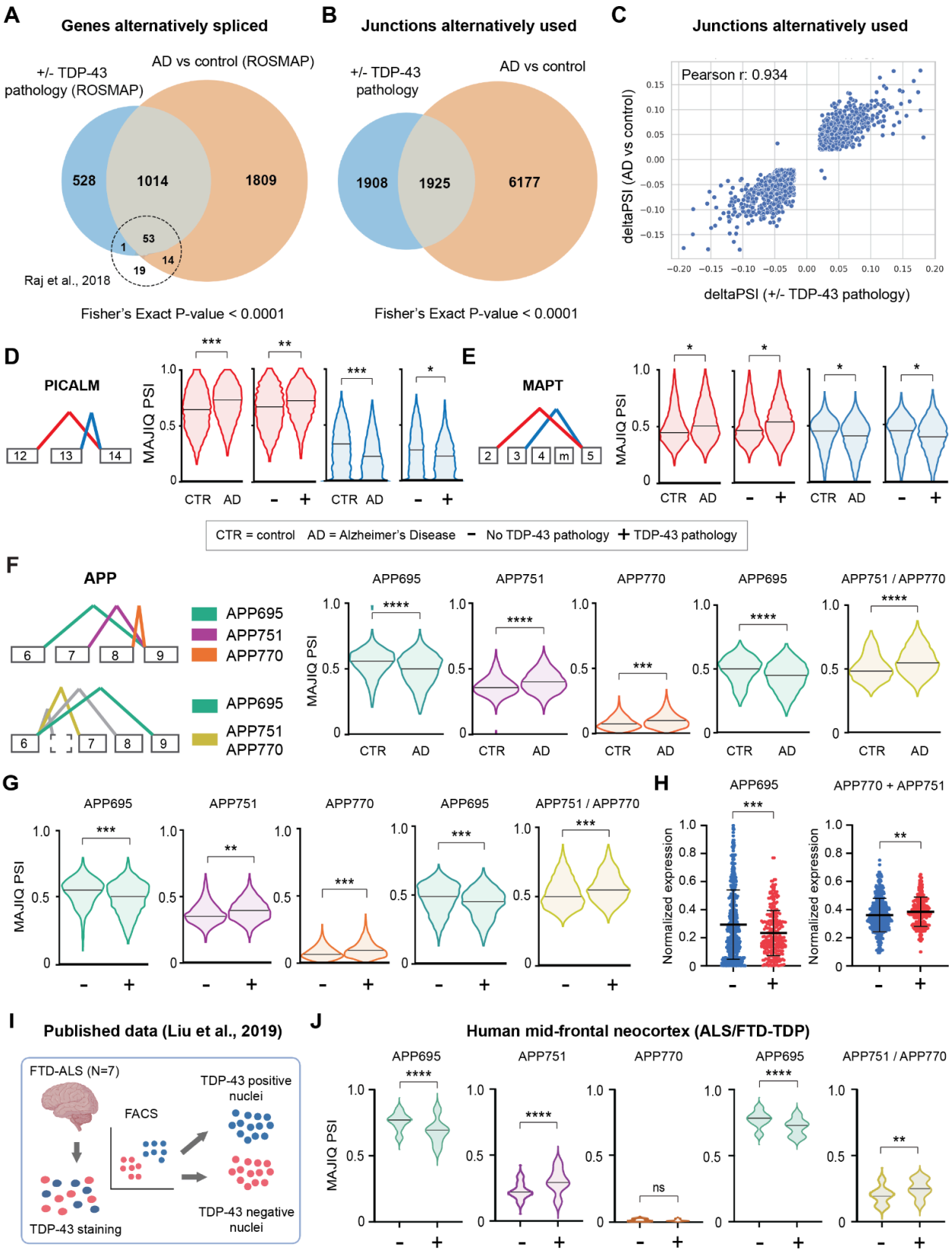
A
Genes alternatively spliced
+/- TDP-43 pathology (ROSMAP)
AD vs control (ROSMAP)
528
1014
1809
1
53
14
19
Raj et al., 2018
Fisher's Exact P-value < 0.0001
B
Junctions alternatively used
+/- TDP-43 pathology
AD vs control
1908
1925
6177
Fisher's Exact P-value < 0.0001
C
Junctions alternatively used
Pearson r: 0.934
deltaPSI (AD vs control)
deltaPSI (+/- TDP-43 pathology)
D
PICALM
12
13
14
MAJIQ PSI
CTR AD - + CTR AD - +
E
MAPT
2
3
4
m
5
CTR = control AD = Alzheimer's Disease - No TDP-43 pathology + TDP-43 pathology
F
APP
6
7
8
9
APP695
APP751
APP770
APP751 / APP770
G
H
Normalized expression
APP770 + APP751
I
Published data (Liu et al., 2019)
FTD-ALS (N=7)
FACS
TDP-43 positive nuclei
TDP-43 staining
TDP-43 negative nuclei
J
Human mid-frontal neocortex (ALS/FTD-TDP)
ns

Figure 1: TDP-43 pathology leads to widespread mis-splicing in Alzheimer's Disease including in amyloid precursor protein (APP). Results of MAJIQ [50] splicing analysis of bulk RNA-seq data from dorsolateral prefrontal cortex (DLPFC) tissue from the ROSMAP study [49], comparing patients clinically diagnosed with AD (N = 253) to controls with no cognitive impairment (N = 201), and comparing brain tissues with TDP-43 pathology (N = 150) to those without (N = 150) (+/- TDP-43 pathology). Venn diagrams display the overlap in **(A)** genes mis-spliced in both analyses (Fisher's Exact P-value < 0.0001) or **(B)** exact MAJIQ splice junctions alternatively used in both comparisons (Fisher's Exact P-value < 0.0001). **(C)** A scatter plot of change in percent spliced in (deltaPSI) per specific splice junction in TDP-43 pathology relative to TDP-43 negative AD brains (x-axis) vs AD pathology relative to controls without cognitive impairment (y-axis). Pearson r = 0.934, P < 0.0001. Schematic of the splice junctions detected by MAJIQ in **(D)** PICALM exons 12-14 and **(E)** MAPT exons 2-5, and corresponding percent spliced-in (PSI) values in ROSMAP AD (N = 253) versus control samples (N = 201) and samples with TDP-43 pathology (+TDP-43, N = 150) versus those without (-TDP-43, N = 150) [48]. Median PSIs per group are indicated. P-values *** < 0.001, ** < 0.01; Wilcoxon test. **(F)** Schematic of the splice junctions detected by MAJIQ in APP exons 6-9 and the corresponding known isoforms and **(G)** corresponding PSI values in ROSMAP samples with TDP-43 pathology (+) versus those without (-). Median PSIs per group are indicated. P-values *** < 0.001, ** < 0.01; Wilcoxon test. **(H)** Normalized APP isoforms expression levels, estimated with RSEM [58,59], of APP695 (without exons 7 and 8) and APP770 (containing exons 7 and 8) in human post-mortem dorsolateral prefrontal cortex (DLPFC), comparing samples without TDP-43 pathology to those with TDP-43 pathology. Lines represent the mean with SD. P-values ****< 0.0001, ***< 0.001, *< 0.05; unpaired two-sided t-test. **(I)** Diagram of the experimental setup of the published study [26] used for splicing analysis. Neuronal nuclei were isolated from ALS/FTLD-TDP brains, stained for TDP-43 and sorted to separate between TDP-43-positive nuclei without pathology and TDP-43-negative nuclei (with pathology). **(J)** MAJIQ percent spliced-in (PSI) values of the APP exons 6-9 splice junctions in TDP-43-positive nuclei without pathology (-) vs TDP-43-negative nuclei (with pathology, +). Data from 7 cases, 35,000 to 100,000 nuclei pre-sorting per case. P-values: ** < 0.01, **** < 0.0001.

In addition, the splice junction between exons 6 and 7 was used 7% more in TDP-43-depleted nuclei, resulting in a relative 1.3-fold increase in isoforms APP751 and APP770 compared to control (P-value < 0.01, **Figure 1J**).

TDP-43 pathology and consequent APP mis-splicing lead to increased amyloid-β pathology

Previous reports have shown a correlation between elevated protein and mRNA levels of KPI(+)APP (APP751 and APP770) and increased amyloid-β (Aβ) production in AD [43–45]. Thus, we examined whether TDP-43 pathology could lead to increased Aβ through APP mis-splicing. First, we tested the correlation between TDP-43 pathology, APP isoforms, and Aβ in human post-mortem brain tissue. ROSMAP DLPFC

samples that displayed TDP-43 pathology also showed increased Aβ pathology (P-value < 0.0001, **Figure 2A**). In addition, binning samples by their ratio of APP770+APP751 over APP695 mRNA levels revealed a correlation between higher (APP770+APP751)/APP695 and elevated Aβ pathology (P-value < 0.05, **Figure 2B, C**). Although this correlation exists regardless of TDP-43 pathology status, the increase in Aβ pathology was larger in the presence of TDP-43 pathology (P-value < 0.0001, **Figure 2D**).

Next, we conducted causal chain mediation analyses to quantify whether APP isoform levels explain part of the relationship between TDP-43 pathology and Aβ pathology in DLPFC samples from the ROSMAP study [48] (**Table 1**). The total effect of TDP-43 on Aβ (noted c) is the overall impact of TDP-43 on Aβ - including both direct (noted c') and mediated effects (noted a and b) - where $c = c' + a \cdot b$. First, we modeled the total effect of TDP-43 on Aβ using linear regression of Aβ over TDP-43 and found that TDP-43 is a significant predictor and positively correlated, explaining 6.5% of the variance in Aβ (coefficient c = 0.4029, P-value < 0.0001). Secondly, the relationship between TDP-43 pathology and different APP isoforms (noted a) is tested: TDP-43 is positively correlated with APP770 levels (coefficient a = 1.874, P-value < 0.0001) and with APP751+APP770 (coefficient a = 0.0465, P-value = 0.003), and negatively correlated with APP695 (coefficient a = -21.8, P-value = 0.005). Positive correlation is also found between TDP-43 and $\frac{APP770}{1+APP695}$ (coefficient a = 0.047, P-value < 0.0001) as well as $\frac{APP571+APP770}{1+APP695}$ (coefficient a = 0.051, P-value = 0.001). Lastly, to estimate mediation effects for the different APP isoforms, the effect of APP on Aβ pathology when controlling for TDP-43 is quantified (**Table 1**). If c' (direct effect of TDP-43 on amyloid beta) is reduced or non-significant when APP is added, then APP mediates the effect. APP770, $\frac{APP770}{1+APP695}$ and $\frac{APP571+APP770}{1+APP695}$ are all mediating the effect of TDP-43 on Aβ, with $\frac{APP770}{1+APP695}$ mediating the largest proportion (0.08, P-value < 0.0001, **Table 1** and **Figure 2E**). No significant mediation effect was found for APP695. Altogether, these results demonstrate that TDP-43 pathology strongly influences Aβ pathology, and that part of this effect is mediated through increased levels of APP770 and APP751 relative to APP695.

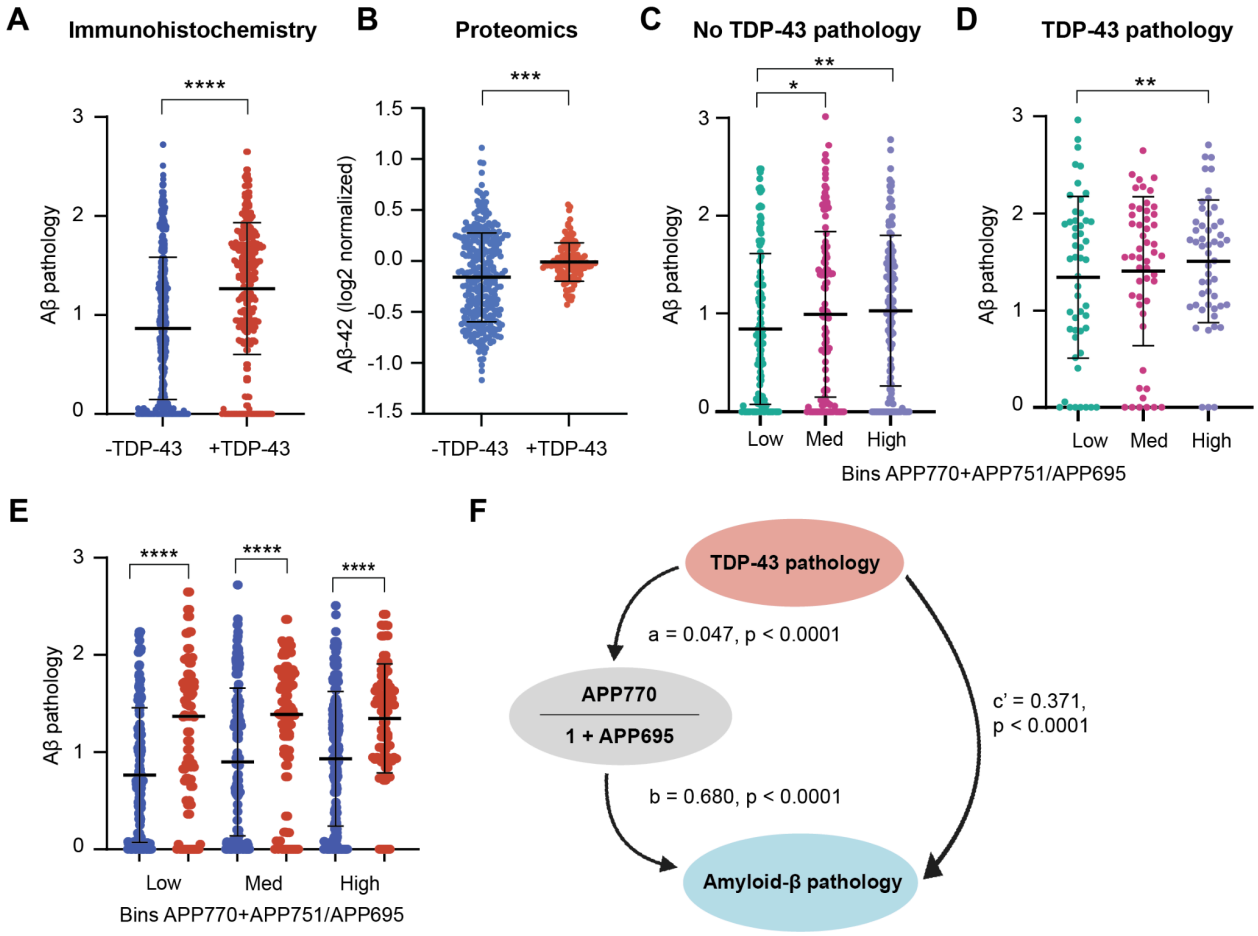

Figure 2: TDP-43 pathology and consequent APP mis-splicing lead to increased Aβ production. Aβ pathology in human DLPFC samples from the ROSMAP study [48] comparing samples with (+) or without (-) TDP-43 pathology as measured by **(A)** immunohistochemistry [60,61] (N=542) or **(B)** mass spectrometry [62] (N=410). Aβ pathology (immunohistochemistry) in human DLPFC samples from the ROSMAP study comparing samples with low, medium or high levels of APP751+APP770 relative to APP695 in **(C)** samples without TDP-43 pathology and **(D)** samples with TDP-pathology, and **(E)** samples with (+) or without (-) TDP-43 pathology binned by levels of APP751+APP770 relative to APP695. Lines and error bars represent mean and standard deviation. P-values ****< 0.0001, ***< 0.001, ** < 0.01, *< 0.05; unpaired two-sided t-test or one-way ANOVA with Dunnett's multiple comparisons test. **(F)** Diagram depicting the results of mediation analysis testing the effect of TDP-43 pathology on Aβ pathology mediated by APP770 levels relative to APP695 levels.

Table 1: Results of mediation analyses testing the effects of TDP-43 pathology and APP isoforms on Aβ pathology.

Hypothesized mediation pathway: TDP-43 $\rightarrow APP \rightarrow$ **Aβ**

Pathway	Equation
TDP-43 → Aβ (without mediation)	$A\beta = \alpha_0 + c \cdot TDP43 + \varepsilon_0$
TDP-43 → APP	$APP = \alpha_1 + a \cdot TDP43 + \varepsilon_1$
$APP \rightarrow A\beta$ (when controlling for TDP-43)	$A\beta = \alpha_2 + c' \cdot TDP43 + b \cdot APP + \varepsilon_2$
Total Effect (c) ≃ Direct effect (c') + Indirect effect ($a \cdot b$) 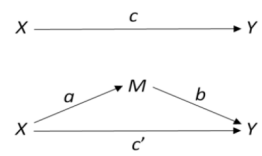	

$APP770$ **as mediator**		
Pathway	**Coefficient**	**P-value**
TDP-43 → Aβ (without mediation)	$c = 0.4029$	0.000
TDP-43 → $APP770$	$a = 1.874$	0.000
$APP770 \rightarrow A\beta$ (when controlling for TDP-43)	$b = 0.0152$ $c' = 0.3742$	0.000, 0.000
Significance of the indirect effect via bootstrapping: $a \cdot b = 0.028$, **95% CI** $[0.012,\ 0.047]$		
Total Effect (c) = 0.429, **direct Effect (c')**= 0.374 $c' < c$ and $c' \neq 0 \Rightarrow APP770$ **is a partial mediator.** **Proportion Mediated** $\frac{(a \cdot b)}{c} = 0.071 = 7\%$.		

$\frac{APP770}{1+APP695}$ **as mediator**		
Pathway	**Coefficient**	**P-value**
TDP-43 → Aβ (without mediation)	$c = 0.4029$	0.000
TDP-43 → $\frac{APP770}{1+APP695}$	$a = 0.0471$	0.000
$\frac{APP770}{1+APP695} \rightarrow A\beta$ (when controlling for TDP-43)	$b = 0.6800$, $c' = 0.3705$	0.000, 0.000
Significance of the indirect effect via bootstrapping: $a \cdot b = 0.032$, **95% CI** $[0.014,\ 0.052]$		
Total Effect (c) = 0.403, **direct Effect (c')**= 0.371 $c' < c$ and $c' \neq 0 \Rightarrow \frac{APP770}{1+APP695}$ **is a partial mediator.** **Proportion Mediated** $\frac{(a \cdot b)}{c} = 0.080 = 8\%$		

$\frac{APP571+APP770}{1+APP695}$ **as mediator**		
Pathway	**Coefficient**	**P-value**
TDP-43 → Aβ (without mediation)	$c = 0.4029$	0.000
TDP-43 → $\frac{APP571+APP770}{1+APP695}$	$a = 0.0512$	0.001
$\frac{APP571+APP770}{1+APP695} \rightarrow A\beta$ (when controlling for TDP-43)	$b = 0.2390$, $c' = 0.3904$	0.020, 0.000
Significance of the indirect effect via bootstrapping: $a \cdot b = 0.012$, **95% CI** $[0.001,\ 0.025]$		
Total Effect (c) = 0.403, **direct Effect (c')**= 0.390 $c' < c$ and $c' \neq 0 \Rightarrow \frac{APP571+APP770}{1+APP695}$ **is a partial mediator.** **Proportion Mediated** $\frac{(a \cdot b)}{c} = 0.030 = 3\%$		

Cytoplasmic gain of toxic function, not loss of nuclear TDP-43 function, leads to APP mis-splicing

We next asked whether the loss of TDP-43 per se is associated with alternative splicing of APP. Analysis of RNA sequencing data of TDP-43 knockdown in iPSC-derived neurons [17] did not reveal aberrant APP splicing (deltaPSI < 0.01, P-values > 0.6), **Figure 3A** and **Supplementary Table 3**). Similarly, no APP mis-splicing was observed upon complete knockout of TDP-43 in HeLa cells [63] (deltaPSI < 0.01, P-values > 0.55, **Figure 3B** and **Supplementary Table 3**). Furthermore, only 16% of the mRNAs that displayed aberrant splicing in TDP-43-negative ALS/FTLD-TDP brain nuclei appear to be affected by TDP-43 knockdown (**Figure 3C**). Therefore, a substantial portion of the splicing changes observed in post-mortem tissues are hard to explain solely by the loss of TDP-43 function and might involve additional molecular mechanisms.

We hypothesized that APP splicing is affected by TDP-43 mislocalization to the cytoplasm, which is a core feature of disease pathology, but is not observed after TDP-43 knockdown. To test this, we overexpressed a TDP-43 construct with a mutagenized nuclear localization signal (NLS) in iPSC-derived neurons (iNs), as described before [64]. As a control, we induced neurons that overexpress a nuclear export signal (NES, **Figure 3D**). The exogenous TDP-43^{deltaNLS} and NES proteins were expressed in the cytoplasm [64]. Next-generation RNA sequencing and splicing analysis (**Supplementary Table 2**) revealed a 32% decrease in the usage of the junction between APP exons 6 and 9 - resulting in the production of APP695 - in TDP-43^{deltaNLS} relative to NES (P-value < 0.0001, **Figure 3E** and **Supplementary Table 3**). In contrast, the

generation of APP751 through the splice junction between exons 7 and 9 was increased to 24% (P-value < 0.0001, **Figure 3E**). Similarly, the junction between exon 6 and 7, leading to APP751 or APP770, is used 32% more (P-value < 0.0001, **Figure 3E**). Quantification of the three major isoforms by reverse transcription PCR (RT-PCR) (**Figure 3F**) orthogonally verified a significant 19% reduction in APP695 and a concomitant increase of 41% in APP751 and 336% in APP770 isoforms in TDP-43^{deltaNLS} (P-values < 0.05, **Figure 3G**). These observations correlate with aberrant APP splicing and TDP-43 pathology in human ALS/FTLD-TDP and AD brains. Finally, about 15% of the genes mis-spliced upon TDP-43 pathology in ALS/FTLD-TDP postmortem tissue [26] were also mis-spliced in TDP-43^{deltaNLS} neurons (**Figure 3H**). This number is in the same ballpark of TDP-43 knockdown models, suggesting toxic gain-of-function through mislocalization substantially contributes to splicing defects in ALS/FTLD-TDP.

The mislocalization of splicing regulators upon cytoplasmic TDP-43

We specifically evaluated the RBPs that were mislocalized to the cytoplasm together with TDP-43 by nucleo-cytoplasmic fractionation and mass spectrometry of induced neurons that expressed either TDP-43^{deltaNLS} or NES. After fractionation by centrifugation, we analyzed the protein content of the two fractions by mass spectrometry (**Figure 4A** and **Supplementary Table 4**). The nuclear proteins Lamin-B1 and HDAC1 were highly enriched in the nuclear fraction of both TDP-43^{deltaNLS} and the control NES cell lines (log2FC = 5.7 / 5.1, FDR = 0; **Supplementary Figure 2A**). In addition, analysis of the top 200 most nuclear enriched or depleted proteins, using the gene ontology database [65,66] confirmed proper separation of the nuclear and cytoplasmic fractions (**Supplementary Figure 2B, C**). TDP-43^{deltaNLS} caused the cytoplasmic enrichment of 173 proteins, relative to the cytoplasm of NES control neurons (FDR < 0.05, FC > 2; **Figure 4B**). TDP-43 itself was among the most enriched proteins with a 6.5-fold higher cytoplasmic expression in TDP-43^{deltaNLS} (FDR = 0.017, **Figure 4B**). Additionally, 20 of the mislocalized proteins are known to be involved in splicing: CELF1 [67–69], CPSF7 [70], CRIPT [71], DDX17 [72–74], DHX16 [75], ERH [76,77], FAM98B [78], HNRNPLL [79–82], LGALS3 [83,84], NONO [85,86], PSPC1 [86], PTBP2 [87], SNRPC [88,89], SRSF1 [90–93], SRSF2 [92–95], SRSF4 [92,93,96], SRSF5 [92,93,97,98], SRSF6 [92,93,97,99], SUPT6H [100] and U2SURP [101,102]. Comparing the cytoplasmic-to-nuclear ratio of these 20 proteins between TDP-43^{deltaNLS} and NES revealed increased cytoplasmic enrichment in TDP-43^{deltaNLS}-expressing neurons (**Figure 4C**). This suggested that additional splicing regulators might be mislocalized to the cytoplasm, together with TDP-43, in human neurons.

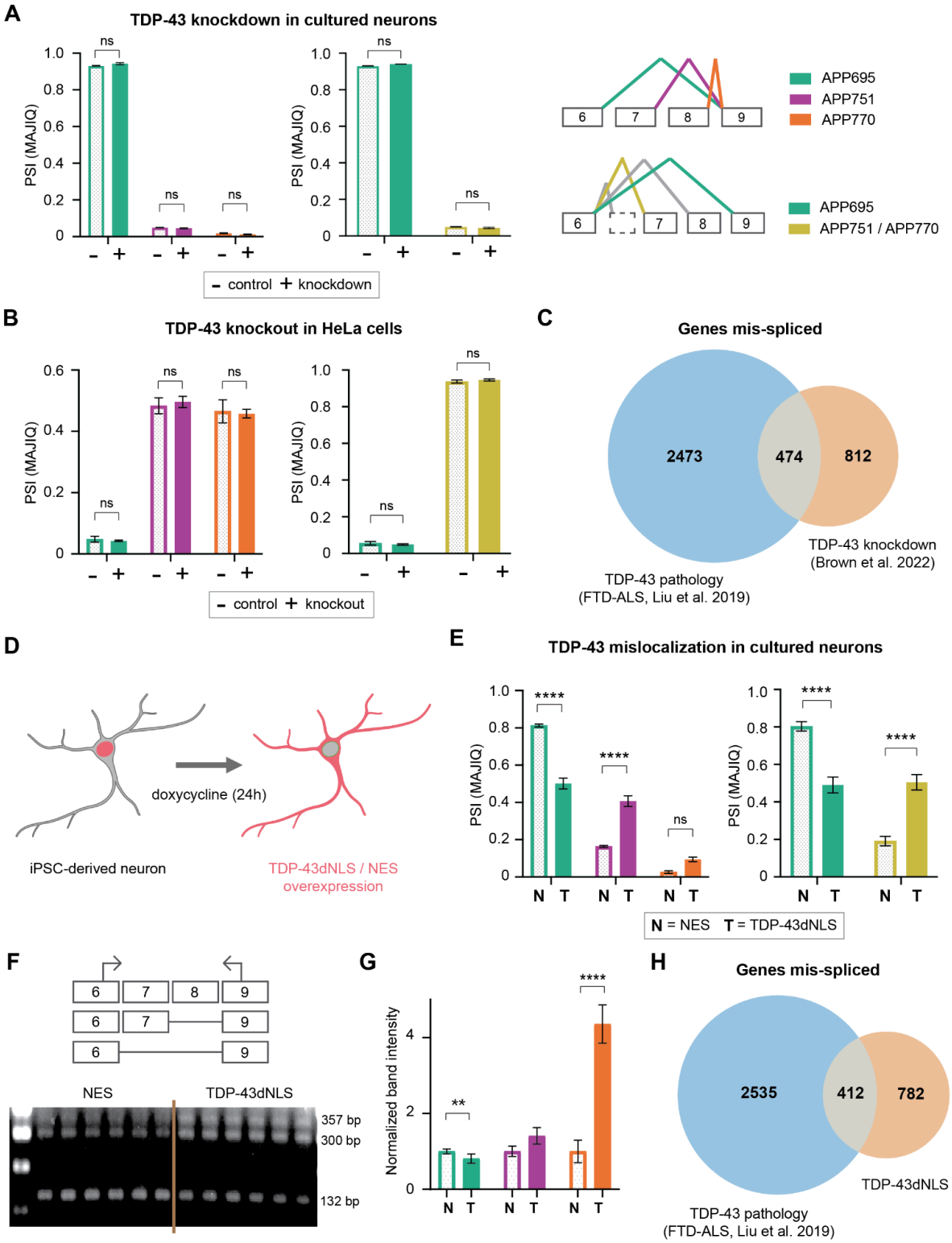
A
TDP-43 knockdown in cultured neurons
PSI (MAJIQ)
ns
- control + knockdown
APP695
APP751
APP770
APP695
APP751 / APP770
B
TDP-43 knockout in HeLa cells
- control + knockout
C
Genes mis-spliced
2473
474
812
TDP-43 knockdown
(Brown et al. 2022)
TDP-43 pathology
(FTD-ALS, Liu et al. 2019)
D
doxycycline (24h)
iPSC-derived neuron
TDP-43dNLS / NES
overexpression
E
TDP-43 mislocalization in cultured neurons
****
**
N = NES T = TDP-43dNLS
F
NES
TDP-43dNLS
357 bp
300 bp
132 bp
G
Normalized band intensity
H
Genes mis-spliced
2535
412
782
TDP-43dNLS
TDP-43 pathology
(FTD-ALS, Liu et al. 2019)

Figure 3: Gain of toxic function of cytoplasmic TDP-43 mislocalization causes APP mis-splicing. Percent spliced in (PSI) of splice junctions corresponding to the 3 main APP isoforms as determined by RNAseq and MAJIQ [50] in **(A)** TDP-43 knockdown in cultured neurons [17], or **(B)** knockout in HeLa cells [63]**. (C)** Venn diagram of alternatively spliced mRNAs in ALS/FTLD-TDP- post-mortem neuronal nuclei displaying TDP-43 pathology [26] and TDP-43 knockdown in cultured neurons [17]. **(D)** Diagram of experimental setup: iPSCs carrying transgenes were differentiated into day 8 cortical neurons [103], at which point NLS-mutated TDP-43 (TDP-43^{deltaNLS}) or nuclear export signal (NES) expression was induced with doxycycline. **(E)** MAJIQ PSI values of splice junctions corresponding to the 3 main APP isoforms in cultured neurons expressing NES or TDP-43^{deltaNLS}. P-values **** < 0.0001. **(F)** Gel of reverse transcription PCR products from APP mRNA isoforms in induced neurons that express either NES or TDP-43^{deltaNLS} and **(G)** corresponding quantification of PCR band intensities (arbitrary units). P-values ****< 0.0001, *< 0.05; unpaired two-sided t-test. **(H)** Venn diagram of alternatively spliced mRNAs in ALS/FTLD-TDP post-mortem neuronal nuclei displaying TDP-43 pathology [26] and in cultured neurons expressing TDP-43^{deltaNLS}.

Probing cytoplasmic interactors of TDP-43 using proximity labeling

To explore the molecular mechanism related to aberrant splicing downstream of cytoplasmic TDP-43 localization, we have characterized the proteins in the vicinity of the cytoplasmic TDP-43. We, therefore, utilized engineered ascorbate peroxidase (APEX), which was part of the TDP-43^{deltaNLS} and NES constructs, to enable proximity labeling (**Figure 4D**). APEX facilitates free radical formation upon exposure to hydrogen peroxide (H2O2), generating biotin-phenol (BP) radicals that attach to neighboring biomolecules. Immunostaining confirmed that the presence of both H2O2 and biotin phenol in the media was essential for biotinylation and that the biotinylation pattern overlapped with the construct localization [64]. In addition, we included sodium arsenite stress as a treatment to model TDP-43 condensation. TDP-43 partially relocalized into biomolecular condensates and co-localized with stress granule marker G3BP1 in induced neurons that were treated with sodium arsenite (250 uM, 90 minutes), (**Supplementary Figure 3**), consistent with previous reports [104–111].

In two independent experiments, biotinylated proteins were purified over streptavidin beads and analyzed by mass spectrometry (MS). Reassuringly, TDP-43 itself was among the most enriched proteins (FDR = 0, log2FC = 5.24) (red dots in **Figure 4E** and **Supplementary Figure 4A**).

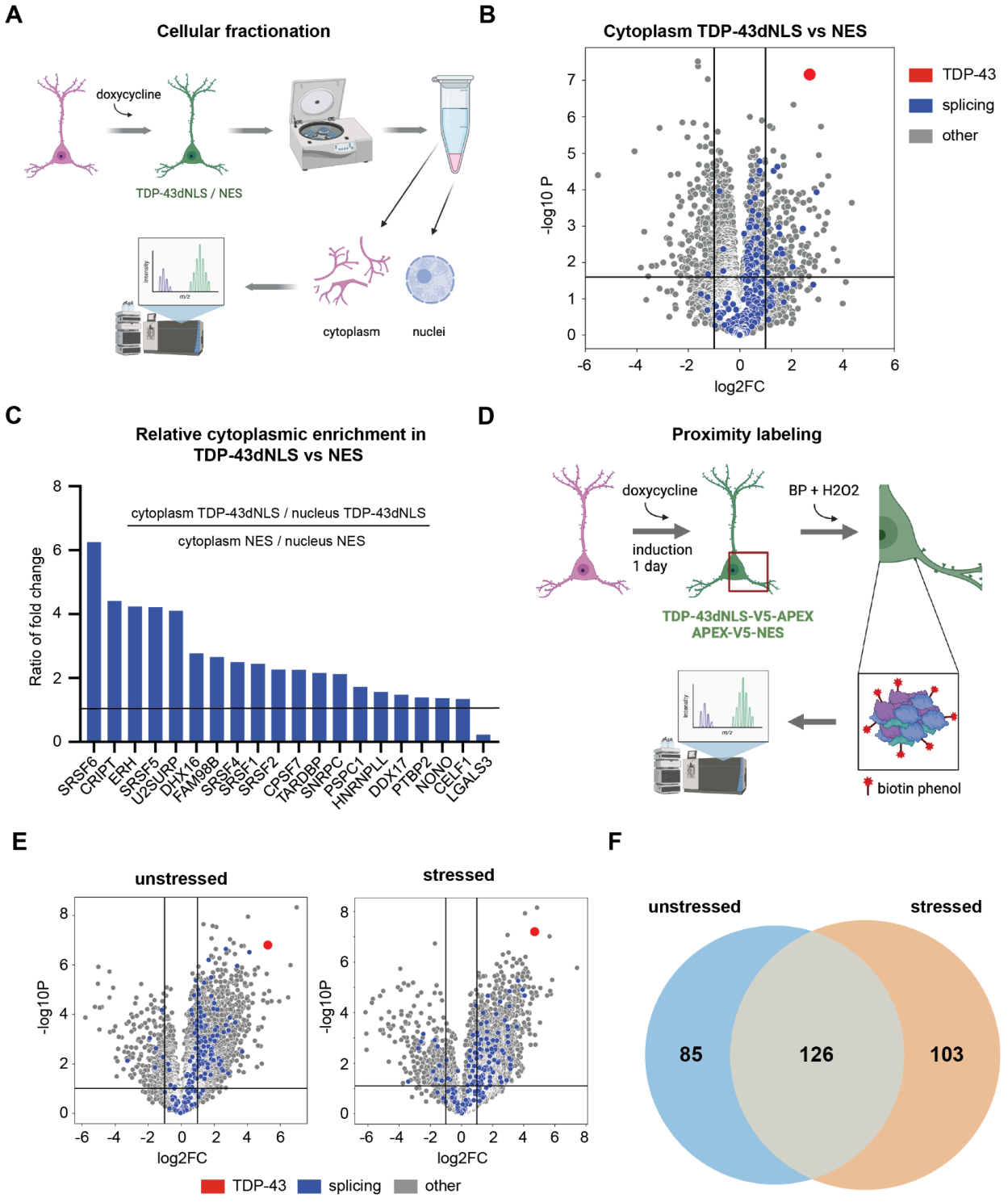

Figure 4: Probing cytoplasmic co-sequestration of splicing factors by TDP-43. (A) Schematic of the subcellular fractionation method to measure protein content of cytoplasmic and nuclear fractions of TDP-43^{deltaNLS}- and NES-expressing neurons. **(B)** Volcano plot depicting protein abundance in the cytoplasm of neurons expressing TDP-43^{deltaNLS} compared to a cytoplasmic control construct (NES). Factors associated with the Gene Ontology term

'splicing' are shown in blue; TDP-43 itself is depicted in red. **(C)** Relative cytoplasmic enrichment of the 14 splicing regulators in TDP-43^{deltaNLS} compared to control NES iNs. For each protein, the ratio of cytoplasmic to nuclear expression in TDP-43^{deltaNLS} was divided to the ratio in NES. **(D)** Schematic of APEX proximity labeling in TDP-43^{deltaNLS}- and NES-expressing neurons. **(E)** Volcano plots of differential protein enrichment in TDP-43^{deltaNLS} samples (right) versus NES samples (left), with TDP-43 shown in red and factors associated with the Gene Ontology term 'splicing' in blue. **(F)** The potential TDP-43 interactors were consistently found in two different experiments in unstressed and/or stressed conditions.

The number of proteins identified varied significantly across experiments. However, at least 211 proteins were detected in both experiments under basal growth conditions and 229 proteins under stress (FDR, < 0.01, log2FC > 2, **Supplementary Table 5**). 126 proteins were consistently associated with cytoplasmic TDP-43 regardless of stress state (**Figure 4F)**. Gene Ontology (GO) pathway molecular function analysis revealed substantial enrichment of DNA- and RNA-binding proteins (**Supplementary Figure 4B**), which aligns with known TDP-43 functions [1,2,112]. This list comprises 65 RBPs that are associated with TDP-43 (**Table 2**), including RBPs that have a role in splicing, e.g., CELF2 [113], TIA1 and TIAL1 [114,115] and HNRNPLL [81].

Table 2: RNA-binding proteins associated with TDP-43^{deltaNLS}.

basal interactors (n=21/65)	interactors under stress only (n=14/65)	interactors under basal or/and stress conditions (n=30/65)
SAMD4B	TTF2	DNMT1
UPF3B	HNRNPLL	SPEN
CELF2	FAM120B	MSI1
DCP2	PAN3	CPSF3
TIAL1	NUP153	DDX24
METTL3	UPF2	YTHDC2
RPS27L	ZCCHC8	LSM14A
HELZ	SPATS2L	AGO1
PDCD11	YTHDF2	AGO2
ZC3H7A	CASC3	RIOK2
EIF3M	G3BP2	TNRC6A
MAZ	SMAD4	MSI2
CNOT10	TSR1	FAM120C
KIAA0430	SUZ12	SMG7

AGO3		TIA1
MKRN2		THUMPD3
PATL1		XPO5
TOP3B		POP1
RBM3		SCAF11
RC3H1		ZC3H11A
HLTF		DCP1A
		G3BP1
		ZC3H12C
		SMG5
		SMG1
		PURB
		TRIM25
		EIF4ENIF1
		PHF6

Knockdown of splicing regulators associated with TDP-43 partially recapitulates TDP-associated changes

We functionally investigated the potential role some of the new interactors of TDP-43 might have in splicing by generating loss of function alleles (knockdown, KD) using a cytidine base editor [116] in human iPSCs that were differentiated to cortical neurons. In total, we identified 90 RBPs in 3 fractionation and proximity labeling experiments. Out of these, we shortlisted 8 factors that are localized mostly to the nucleus under basal conditions and are reported to be involved in splicing: CELF2 [117–121], CPSF7 [70], HNRNPLL [79–82], SCAF11 [122], SRSF5 [92,93,97,98], SUPT6H [100], TIA1 [114,115,123] and TIAL1 [123–125] (**Figure 5A**). TIA1 was included because of its genetic association with ALS [126,127], and TIAL1 is its paralog and acts in close coordination [123,125,128,129]. The introduction of premature stop codons prevented the formation of full-length protein products and led to downregulation of mRNA levels **(Supplementary Figure 5**). Full RNA sequencing followed by splicing analysis revealed differential usage (|deltaPSI| > 0.1, P-value < 0.1) of hundreds of splice junctions upon RBP knockdown (**Table 3** and **Supplementary Table 2**). TIA1 displayed the mildest phenotype, likely since it was the only heterozygous KD (generation of a homozygote was unsuccessful) (**Table 3**).

Interestingly, UNC13A was misspliced upon SRSF5 and SUPT6H KD (**Figure 5B**), although in a different manner than reported previously [16,17]. In SRSF5 KD neurons, two events were significantly altered: one mapping to canonical exon 7 and an unannotated exon identified by MAJIQ (hg38; chr19:17665549-17665977, |deltaPSI| = 17%, P-value < 0.05), and another involving exon 37 and canonical exon 39 (hg38; chr19:17623118-17623263, |deltaPSI| = 20%, P-value < 0.05) (**Supplementary Figure 6A**). The same mis-splicing in exon 7 and an annotated exon occurred upon SUPT6H KD (|deltaPSI| = 18%, P-value < 0.05, **Supplementary Figure 6B**). Each of these events was relatively rare, with only a few dozen reads mapping to each junction. No alternative splicing of STMN2 was detected in any of the KD lines (**Figure 5B**).

Table 3: Number of splice junctions with significantly different usage between conditions (|deltaPSI| > 0.1, P-value < 0.1).

Condition	N junctions more included	N junctions less included
SRSF5 knockdown (-/-)	2656	2708
CPSF7 knockdown (-/-)	1666	1574
SUPT6H knockdown (-/-)	1533	1559
TDP-43 knockdown	1528	1564
TIAL1 knockdown (-/-)	1108	1120
CELF2 knockdown (-/-)	950	943
HNRNPLL knockdown (-/-)	903	923
SCAF11 knockdown (-/-)	870	934
TIA1 knockdown (+/-)	691	645

When comparing the significantly mis-spliced genes (|deltaPSI| > 0.1, P-value < 0.1 in at least one junction) across all conditions, all RBPs have at least a hundred and sometimes several hundreds of splice targets in common with TDP-43 pathology (**Figure 5C**). A substantial fraction of the splicing events that are associated with TDP-43 pathology in post-mortem tissue are also observed as a consequence of the loss of specific splicing regulators that are associated with cytoplasmic TDP-43. For example, 20% of the mRNAs that were mis-spliced in ALS/FTLD-TDP tissues are also alternatively spliced upon SRSF5 KD (585 out of 2947 mRNAs, Fisher's Exact P-value < 0.0001, **Figure 5C**). These results suggest that mislocalization of TDP-43 to the cytoplasm leads to splicing defects not only because of the loss of TDP-43 function from the nucleus but at least in part because of the loss of other splicing regulators from the nucleus.

Knockdown of TDP-43-associated splicing factors leads to APP mis-splicing and Aβ generation

We next examined whether the loss of TDP-43-associated splicing regulators could cause the APP mis-splicing observed upon cytoplasmic TDP-43 mislocalization (**Figure 3E**). Indeed, the inclusion of APP exons 7 and 8 was increased upon knockdown of TIAL1, SCAF11, and SRSF5 (P-values < 0.05, **Figure 5D** and **Supplementary Table 3**), similar to what was observed in ALS/FTLD-TDP brains (**Figure 1G, I**). This was orthogonally verified with RT-PCR (P-values < 0.05, **Figure 5E**). TIAL1 was shown to bind to APP mRNA [130], which supports a function in APP splicing (SCAF11 and SRSF5 were not tested). These results suggest that TDP-43 mislocalization and co-sequestration of other splicing regulators changes the balance between APP isoforms towards APP751 and APP770.

Finally, we stained cultured neurons for Aβ (**Figure 5F**) and observed increased cytoplasmic Aβ intensity in TIAL1 and SCAF11 KD neurons compared to control (P-values < 0.001 and < 0.0001, respectively, **Figure 5G**). Furthermore, the number of Aβ-positive puncta was increased in all three KD lines (P-values < 0.05, **Figure 5H**).

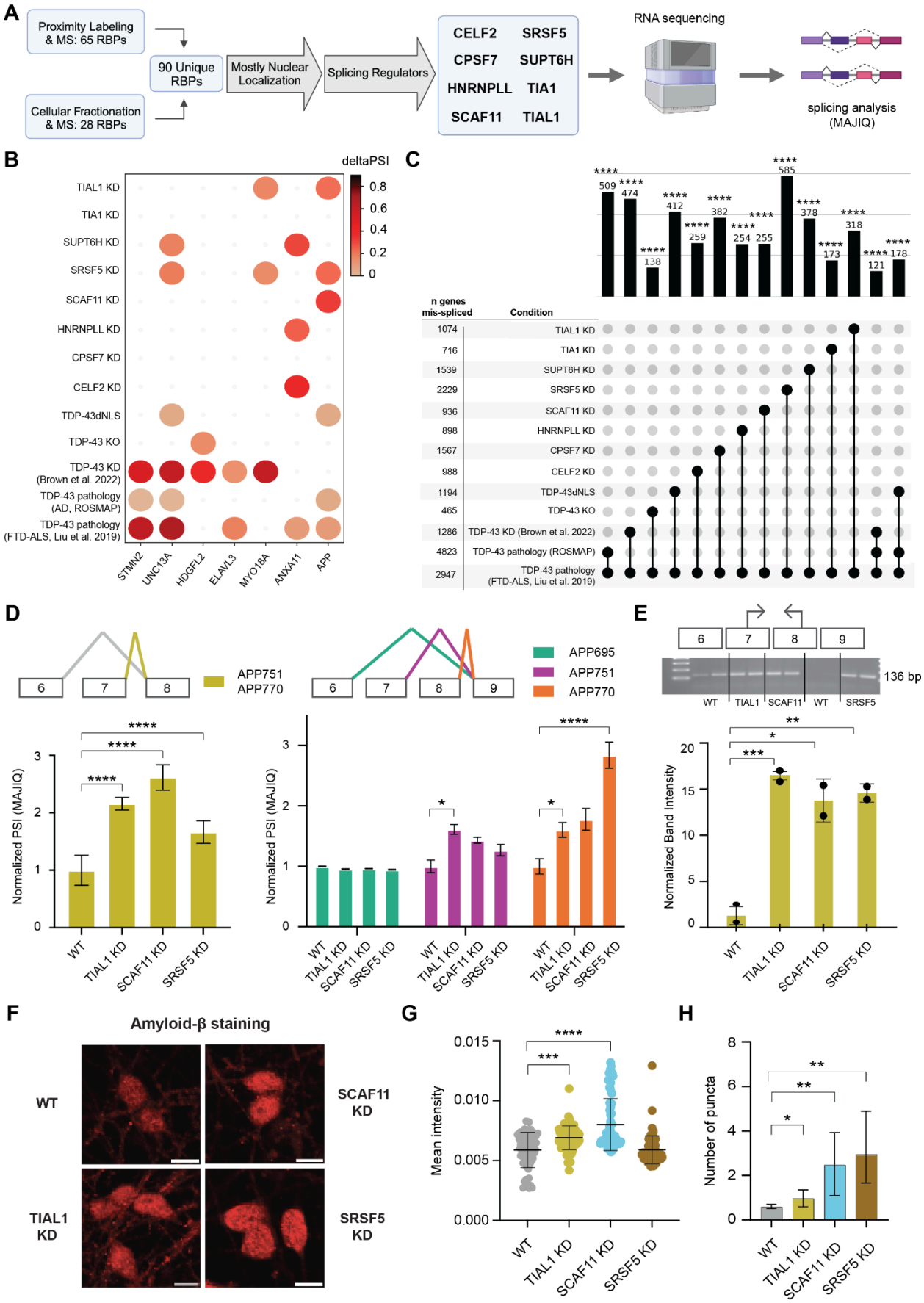
A
Proximity Labeling & MS: 65 RBPs
Cellular Fractionation & MS: 28 RBPs
90 Unique RBPs
Mostly Nuclear Localization
Splicing Regulators
CELF2 SRSF5
CPSF7 SUPT6H
HNRNPLL TIA1
SCAF11 TIAL1
RNA sequencing
splicing analysis (MAJIQ)
B
deltaPSI
TIAL1 KD
TIA1 KD
SUPT6H KD
SRSF5 KD
SCAF11 KD
HNRNPLL KD
CPSF7 KD
CELF2 KD
TDP-43dNLS
TDP-43 KO
TDP-43 KD (Brown et al. 2022)
TDP-43 pathology (AD, ROSMAP)
TDP-43 pathology (FTD-ALS, Liu et al. 2019)
STMN2
UNC13A
HDGFL2
ELAVL3
MYO18A
ANXA11
APP
C
n genes mis-spliced
Condition
D
APP751
APP770
APP695
Normalized PSI (MAJIQ)
WT
TIAL1 KD
SCAF11 KD
SRSF5 KD
E
136 bp
Normalized Band Intensity
F
Amyloid-β staining
WT
SCAF11 KD
TIAL1 KD
SRSF5 KD
G
Mean intensity
H
Number of puncta

Figure 5: Knockdown of TDP-43-associated splicing factors partially recapitulates ALS/FTLD-TDP-associated changes. (A) Schematic overview of the steps prioritizing 8 splicing factors for knockdown in iPSCs. **(B)** Percent change spliced in (deltaPSI) per splice junction as determined by MAJIQ in knockdown neurons compared to control. Significant events in UNC13A, UNC13B, STMN2, APP, and the genes knocked out are annotated. **(C)** Comparison of splicing changes across conditions. Numbers on the left indicate the total number of genes alternatively spliced, and numbers on the top indicate the number of genes present in the dataset(s) colored in black. P-values **** < 0.0001, Fisher's Exact Test comparing the significantly mis-spliced genes in each dataset with those in TDP-43 pathology [26]. In the comparisons of three groups, a hypergeometric test was applied. **(D)** Alternative splicing of exons 6-9 of the APP mRNA as determined by MAJIQ in different knockdown neurons compared to control. Plots display percent spliced in (PSI) values normalized to control per junction. P-values * < 0.1, **** < 0.001. **(E)** Gel of reverse transcription PCR products from APP mRNA isoforms in induced neurons corresponding quantification of PCR band intensities (arbitrary units). **(F)** Representative images of Aβ immunofluorescent staining in iPSC-derived neurons knocked out for TIAL1, SCAF11 or SRSF5. Corresponding quantification of **(G)** mean cytoplasmic intensity and **(H)** number of puncta normalized by cell number. Data from 3 repeats, 25 images per repeat are plotted; each point represents the average per **(G)** image or **(H)** well. P-values * < 0.05, ** < 0.01, *** < 0.001, **** < 0.0001.

Discussion

Our study demonstrates that TDP-43 pathology is broadly associated with splicing alterations in AD, including in the amyloid precursor protein (APP) gene. Both in AD and ALS/FTLD-TDP, TDP-43 pathology shifts the isoform balance towards APP751 and APP770, thus establishing a new and unexpected connection across different neurodegenerative disorders. We show that this splicing alteration correlates with increased amyloid-β (Aβ) pathology, providing molecular evidence linking TDP-43 pathology to APP dysregulation and amyloid pathology. Functional validation using iPSC-derived neurons confirmed that cytoplasmic TDP-43 sequestration, rather than nuclear depletion, drives APP mis-splicing, suggesting an orthogonal but compatible mechanism to previously reported [13,16,17,20] loss of nuclear TDP-43 function. Finally, we report several RNA-binding proteins (RBPs) co-sequestered with TDP-43 that potentially contribute to this dysregulation.

While TDP-43 proteinopathy was first linked with ALS and FTD [3], the presence of TDP-43 pathology in up to 57% of AD cases [6,131] and dysregulated TDP-43 in Huntington's disease (HD) [23] underscores its role in neurodegeneration. Abnormal levels or subcellular distribution of TDP-43 contributes to neuronal loss [105,132,133], and in AD, TDP-43 pathology correlates with worsened cognitive decline [134] and severity of pathology [135]. Thus, TDP-43 dysfunction might be a key contributor to neurodegenerative diseases.

Splicing dysregulation is emerging as an important causal mechanism, leading to neurodegeneration in diverse neurodegenerative diseases. Splicing defects in AD have been documented previously [27–33] and offer a mechanistic explanation for genetic variants in novel and known AD genes, including APP [27]. However, the upstream causes remained unclear. Our data suggest that TDP-43 pathology is a significant driver of splicing abnormalities in AD, including in AD-implicated genes.

APP alternative splicing has been recognized for decades [41,42], but the underlying mechanism remained unclear. Our study provides a molecular handle on the regulation of APP splicing downstream of dysregulated TDP-43 in both ALS/FTLD-TDP- and AD.

Through mediation analysis, we show that TDP-43 pathology is associated with increased Aβ production, both directly and indirectly via shifting APP isoform towards APP751/770. This is consistent with initial results from an AD mouse model, where injection of TDP-43 into the hippocampus increased amyloid plaques and impaired spatial memory [9], and data from a small human cohort in which KPI(+)APP correlated with neuritic plaque density [47]. In addition, previous *in vitro* results showed increased Aβ

production upon transfection with the longer APP isoforms compared to APP695 [136]. This discovery offers a molecular explanation for increased amyloid burden in TDP-43-positive AD cases [137,138]. Given that TDP-43 pathology is found in a significant subset of AD patients, this mechanism could have broad implications for understanding and treating AD.

TDP-43-associated splicing pathology has been recently suggested to involve a loss-of-function mechanism due to nuclear depletion [13,16,17,20]. Our data suggests a non-mutually exclusive role for toxic cytoplasmic gain-of-function. We demonstrate that TDP-43 mislocalization does not necessarily disrupt APP splicing directly, but rather due to sequestration of other splicing regulators, such as SRSF5/TIAL1/SCAF11. This contrasts with STMN2 and UNC13A mis-splicing, which directly results from nuclear TDP-43 depletion. The interplay between these two mechanisms highlights the complexity of TDP-43 pathology. Future therapeutic strategies should consider targeting both nuclear restoration and cytoplasmic toxicity to mitigate TDP-43-driven neurodegeneration.

Dysregulation of splicing regulators due to TDP-43 pathology provides a mechanistic explanation for widespread splicing defects in neurodegenerative diseases. Loss of TDP-43 function through knockdown and gain-of-function through mislocalization in culture each explain about 15% of the mis-splicing associated to TDP-43 pathology in ALS/FTLD-TDP postmortem tissue [26], suggesting that both mechanisms can comparably contribute to splicing dysregulation downstream of TDP-43.

Furthermore, correction of splicing has been utilized as a therapeutic approach [139–141], and correction of STMN2 and UNC13A splicing is being developed as a potential intervention strategy [142,143]. Therefore, redirecting APP splicing towards APP695 in the expanse of APP751/770 might be a justified therapeutic strategy as well.

Limitations: While our study provides strong evidence for TDP-43's role in APP splicing, several limitations should be noted. Although we identify cytoplasmic splicing regulators co-sequestered with TDP-43, their direct contributions to APP mis-splicing require further exploration. In addition, additional splice factors not identified in this study may contribute to APP splicing regulations.

Our study identifies a novel mechanism linking TDP-43 pathology to APP alternative splicing and amyloid pathology in AD and supports the concept that TDP-43 pathology serves as a unifying molecular feature linking seemingly disparate neurodegenerative disorders. We provide evidence that TDP-43

mislocalization leads to cytoplasmic sequestration of splicing regulators, driving an increase in APP751 and APP770 isoforms. This mechanism underlying TDP-43 dysfunction suggests that ALS and FTD and amyloid-driven pathology in AD may share common underlying molecular mechanisms. By establishing TDP-43 as an upstream regulator of APP splicing, our findings offer new insights into the molecular convergence of neurodegenerative diseases. Further work will be needed to determine whether these convergences occur early in the evolution of these diseases or are a late common consequence of diverse causes of chronic CNS neurodegeneration. Targeting this pathway may present novel therapeutic opportunities for both ALS/FTLD-TDP and AD, highlighting the broader impact of splicing dysregulation in neurodegeneration.

Supplementary Figures

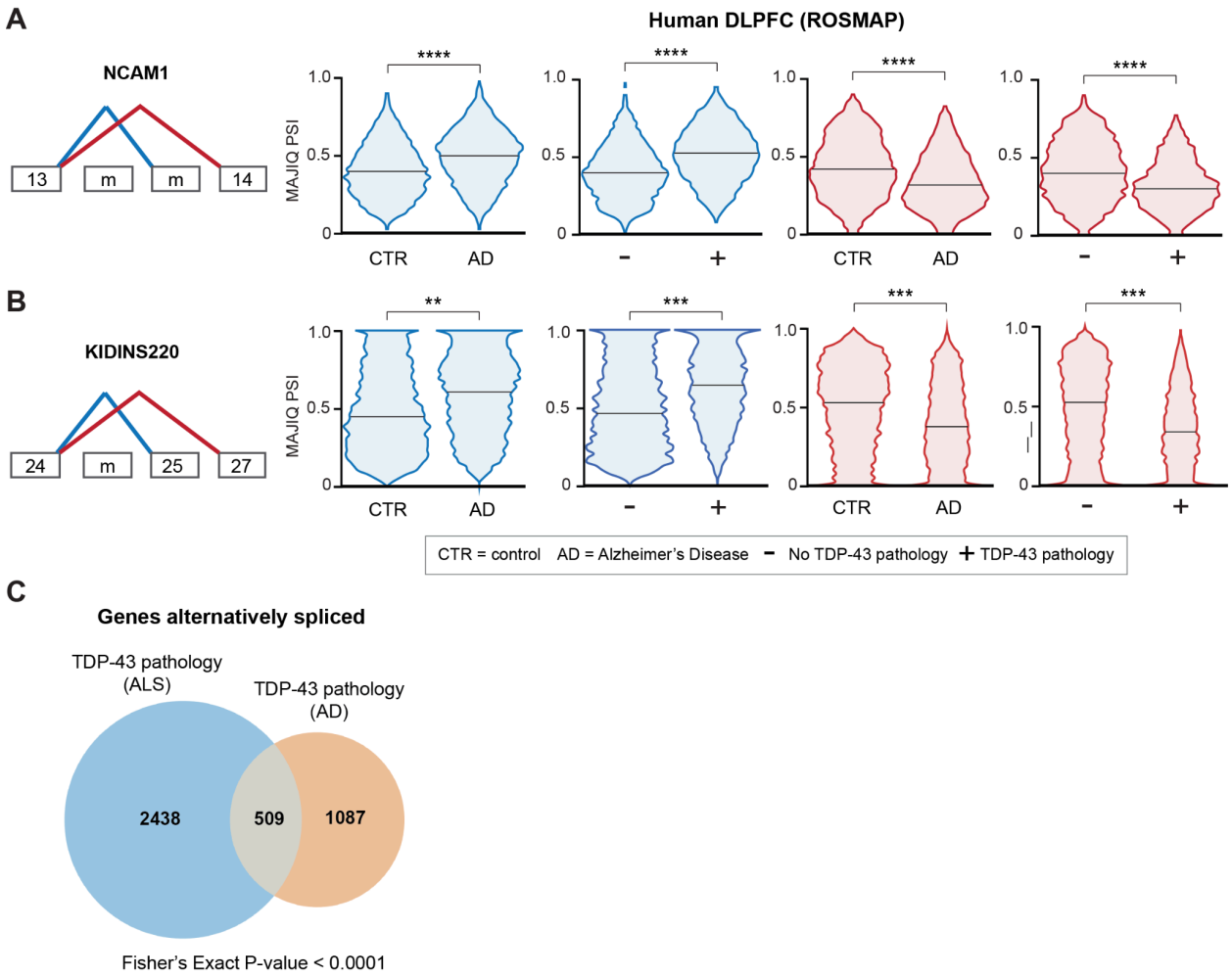

Supplementary figure 1: Splicing aberrations downstream of TDP-43 pathology in human post-mortem tissue. Schematic of the splice junctions detected by MAJIQ in **(A)** NCAM1 exons 13-14 and **(B)** KIDINS220 exons 24-27, and corresponding percent spliced-in (PSI) values in ROSMAP AD versus control samples and samples with TDP-43 pathology (+TDP-43) versus those without (-TDP-43) [48]. Numbers in the schematic indicate canonically annotated exons, and 'm' represents novel exons identified by MAJIQ. Median PSIs per group are indicated. P-values **** < 0.0001, *** < 0.001, ** < 0.01; Wilcoxon test. **(C)** Overlap in genes mis-spliced in TDP-43 depleted nuclei vs TDP-43-positive nuclei from post-mortem cortical tissue [26] and genes mis-spliced upon TDP-43 pathology in ROSMAP DLPFC samples.

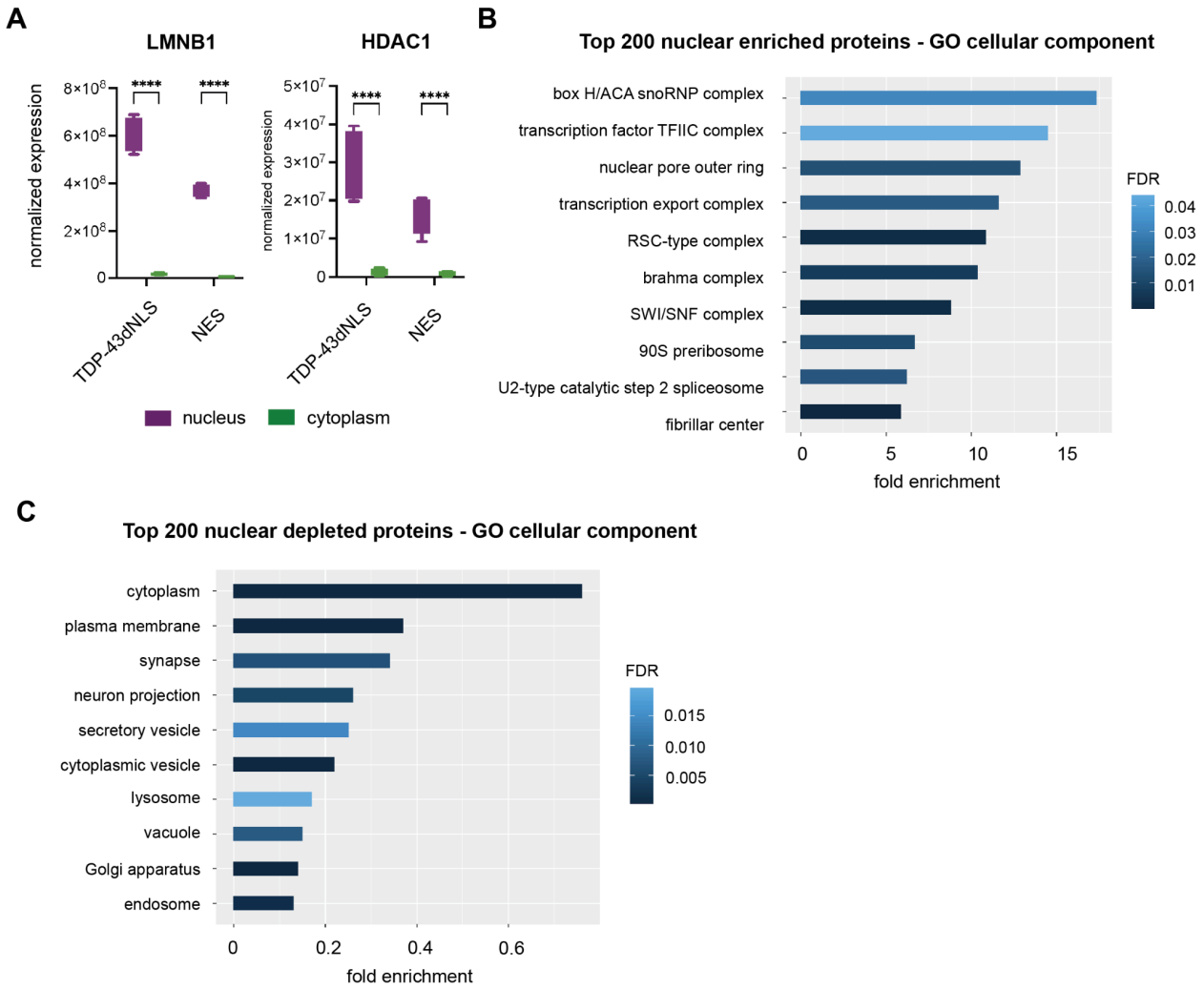

Supplementary Figure 2: Validation of separation between nuclear and cytoplasmic fractions. (A) Relative LMNB1 and HDAC1 intensity in each of the fractions in either NES- or TDP-43^{deltaNLS}-expressing neurons. Gene ontology [65,66] cellular component analysis of the top 200 most nuclear **(B)** enriched or **(C)** depleted proteins.

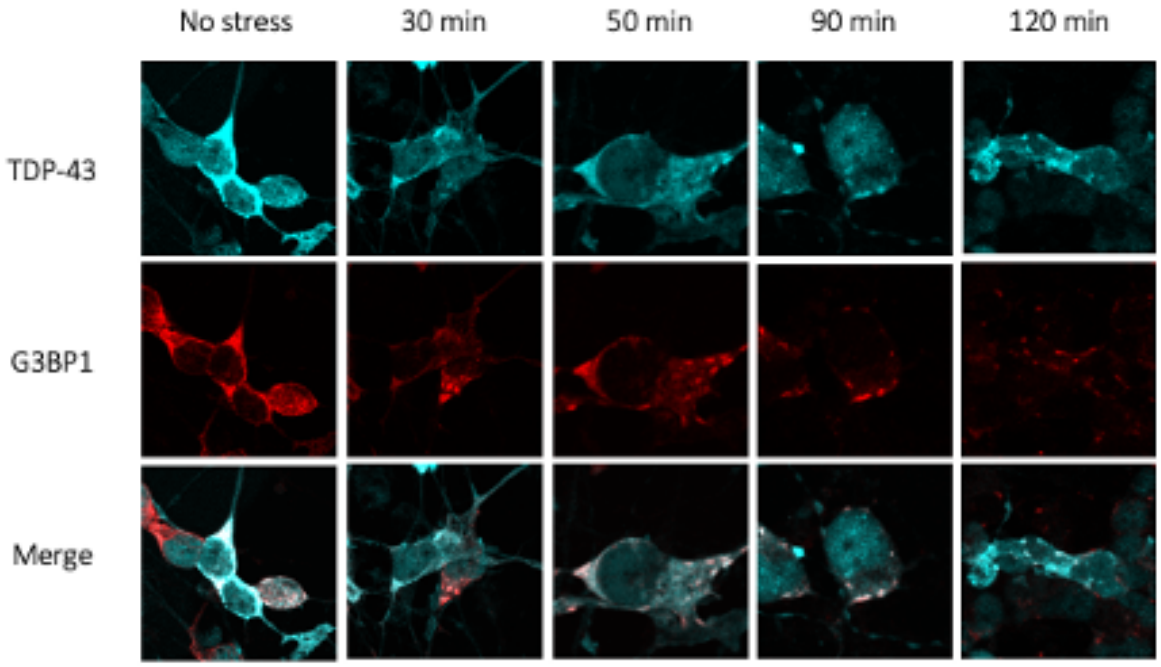

Supplementary Figure 3: Subcellular distribution of TDP-43dNLS under different time points of sodium arsenite stress. Immunostaining of neurons expressing TDP-43dNLS-V5-APEX in different time points after sodium arsenite addition.

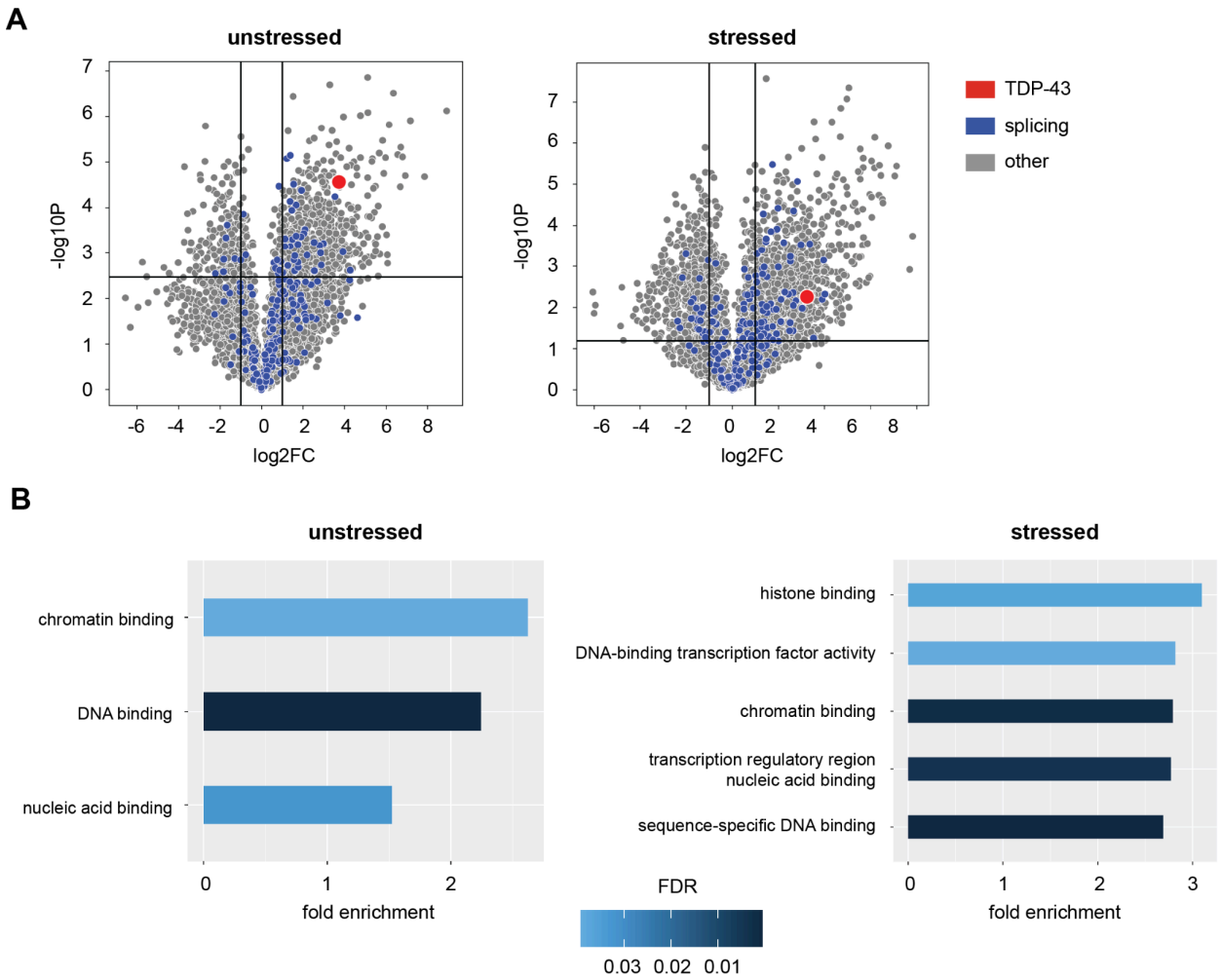

Supplementary Figure 4: Proximity labeling proteomics to map protein interactors of TDP-43^{deltaNLS}. (A) Volcano plots of differential protein enrichment in TDP-43^{deltaNLS} samples versus NES samples, without (left) or with (right) addition of sodium arsenite stress. TDP-43 is shown in red and factors associated with the Gene Ontology term 'splicing' in blue. **(B)** Gene ontology [173,174] molecular function analysis of proteins enriched in TDP-43^{deltaNLS} samples versus NES samples.

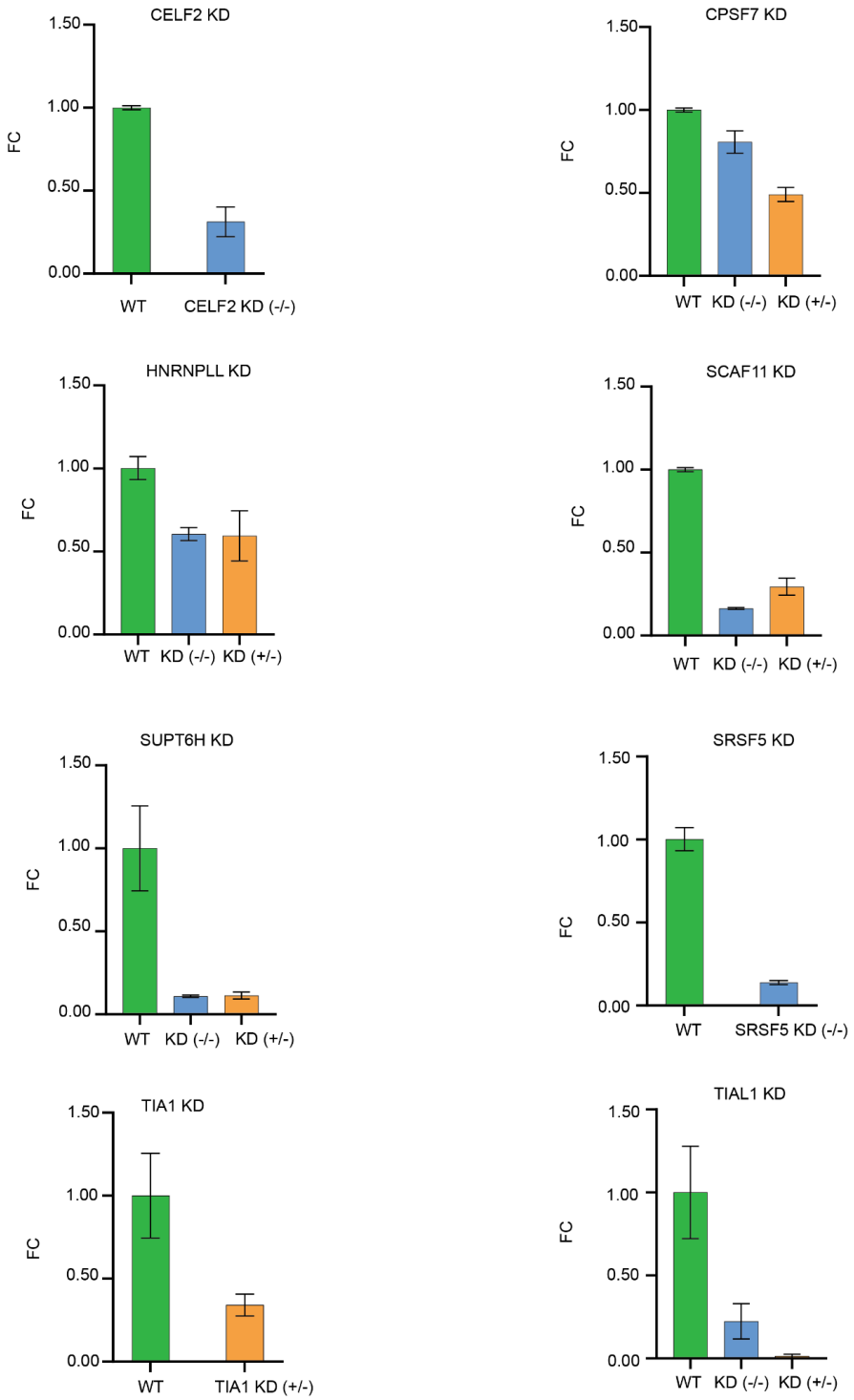

Supplementary Figure 5: Validation of RBP knockdown by qPCR. Relative RNA fold change (FC) in knockdown (KD) iPSCs compared to control.

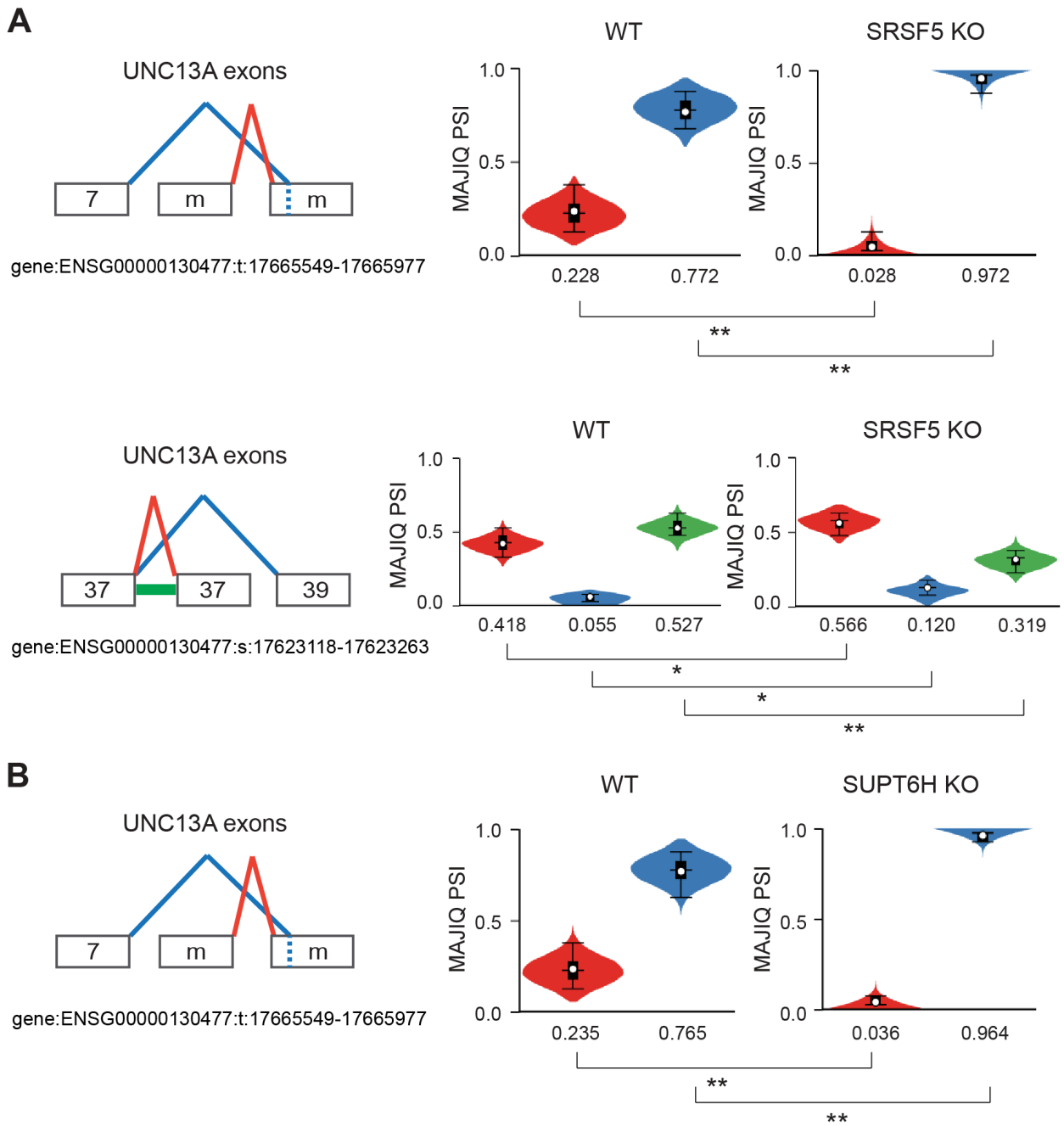

Supplementary Figure 6: Alternative splicing of UNC13A upon SRSF5 and SUPT6H knockdown. (A) Output of MAJIQ deltaPSI analysis comparing WT and **(A)** SRSF5 or **(B)** SUPT6H KD neurons, displaying the two events in UNC13A that were significantly altered. Numbers indicate canonically annotated exons, and 'm' represents exons identified by MAJIQ. P-values: * < 0.1, ** < 0.05.

Materials and methods

Published AD and ALS/FTLD-TDP datasets

For analysis of AD and control brain tissues with and without TDP-43 pathology, we included bulk RNA-seq data from dorsolateral prefrontal cortex (DLPFC) samples from the Religious Orders Study and Rush Memory and Aging Project (ROSMAP) [48] available in Synapse (syn3388564). All participants in ROSMAP were enrolled without known dementia and agreed to annual clinical evaluation and brain donation. Both studies were approved by an Institutional Review Board of Rush University Medical Center. Each participant signed informed and repository consents and an Anatomic Gift Act. Raw bam files (syn4164376) from 300 samples (150 with and 150 without TDP-43 pathology, to approximate the real distribution in patients [5,6]) were used as input for splicing analysis described below. Normalized isoform-level expression data (syn3505746) as determined by RSEM [58] from 505 samples was used as orthogonal verification. When comparing samples without TDP-43 pathology to those with TDP-43 pathology, TDP-43 stage (tdp_st4) was dichotomized as per RADC recommendation: no pathology = no TDP-43 pathology or TDP-43 pathology in amygdala only (Stages 0 and 1); TDP-43 pathology = TDP-43 pathology extending beyond amygdala (Stages 2 and 3) [144,145]. To compare the expression of APP isoforms, we applied a min–max normalization, which scales expression values so that each isoform's minimum and maximum levels correspond to 0 and 1, respectively. We then compared each isoform (APP695, APP751, APP770) individually as well as the sum of the pathogenic isoforms (APP751 + APP770) relative to the canonical APP695 isoform. For measurements of Aβ pathology, we used the RADC amylsqrt_est_8reg variable, reflecting mean amyloid score across 8 brain regions [60,61].

Proteomic data of ROSMAP DLPFC tissues was generated as in [62].

For analysis of human autopsy brain tissues from ALS/FTLD-TDP patients, we used existing RNA-seq data as published in [26]. Briefly, nuclei from mid-frontal neocortical brain tissue from 7 patients diagnosed with FTLD-TDP (all carrying C9orf72 hexanucleotide repeat expansions) were isolated and stained for DAPI, NeuN and TDP-43. Using flow cytometry, nuclei with pathological loss of TDP-43 were separated from TDP-43-positive nuclei. Sorted nuclei were then subjected to RNA extraction and Illumina sequencing as described [26].

Human iPSC culture

Human iPSCs were grown in mTeSR1 (STEMCELL Technologies, 85850) or mTeSR Plus (STEMCELL Technologies, 100-0276) medium at 37°C with 5% CO2 on tissue culture dishes coated with Geltrex (A1413302, Gibco) or Corning Matrigel (Sigma-Aldrich, CLS354277). Coating was done overnight or for at least 1 hour at 37°C. Cell culture medium was exchanged daily (mTeSR1) or every two days (mTeSR Plus). When reaching ~80% confluency, iPSCs were dissociated with accutase (ThermoFisher Scientific, A1110501) and plated in mTeSR1 containing ROCK inhibitor Y-27632 (10 µM, Tocris Bioscience, 1254). For freezing, cells were resuspended in mTeSR1 supplemented with 30% KnockOut Serum Replacement (ThermoFisher Scientific, 1082802) and 10% DMSO.

Generation of inducible TDP-43^{deltaNLS} and NES APEX iPSC lines

We generated iPSC lines based on iW11-NGN2 (gift from Michael Ward) carrying a doxycycline-inducible APEX construct fused to either NLS-mutated TDP-43 (TDP-43^{deltaNLS}) or nuclear export signal (NES) as cytoplasmic control. Constructs also included a V5 tag for visualization by microscopy. Constructs were cloned into the PG-TO-hNGN2 plasmid (gift from Michael Ward, Addgene plasmid #172115) in the place of NGN2, after which the cassettes were integrated into the genome via the piggybac transposon system as described previously [64]. Briefly, iPSCs were seeded into a 6-well plate 12-24 hours prior to transfection. APEX-containing cassettes were mixed with Opti-MEM I Reduced-Serum Medium (Gibco 31985-047) and TransfeX Transfection Reagent (ATCC® ACS-4005™) along with piggyBac™ transposase vector and incubated at room temperature for 15-30 minutes. A total of 2µg of DNA was introduced per well, with a donor-to-transposase ratio of 2:1. Cells were then incubated at 37°C with 5% CO_2 for 24 hours. At 24 hours post-transfection, medium was replaced with medium containing 0.4 µg/ml of puromycin (InvivoGen ant-pr-1). Puromycin-containing medium was replaced daily for 2-3 days until only BFP-expressing cells remained in the culture. From the resulting polyclonal pools, we carefully selected clones. Induction of APEX constructs was achieved by adding doxycycline (2 µg/ml) for 4 (NES) or 24 (TDP-43^{deltaNLS}) hours.

Generation of knockdown iPSC lines

KOLF2.1J human iPSCs [146] were genetically edited with a BE3 cytidine base editor [116] as described previously [147] with minor adjustments. Guide RNAs were designed with the CRISPR design tool in Benchling to generate premature stop codons and cloned into the pKLV2 gRNA plasmid (Addgene plasmid #67974) using Gibson assembly (NEB). DNA sequences of all guides and primers used for

amplifying and sequencing the target region are listed in **Supplementary Table 6**. For each gene target, the top off-target site was amplified and sequenced to verify the absence of off-target edits (see **Supplementary Table 6** for primer sequences). For transfection, 0.5 million iPSCs were seeded into a well of a 6-well plate. The next day, medium was replaced with mTeSR1 supplemented with Rock inhibitor (10 μM). Per reaction, 1 μg of iBE3 CLYBL base editor plasmid (Addgene plasmid #174569) and 1 μg of guide plasmid were introduced with TransfeX as described above. Cells were then incubated at 37°C with 5% CO_2 for 24 hours. The two days after transfection, medium was replaced with medium containing puromycin (0.8 μg/ml) and doxycycline (2 μg/ml) each day. On the third day post-transfection, cells were dissociated and seeded into a matrigel-coated 96-well plate at a concentration of 1 cell per well through serial dilution. Cells were grown for ~2 weeks as described above until wells were full, with daily medium replacements with Rock inhibitor for the first 2-3 days. After this, medium was replaced once every two days with mTeSR1 without Rock inhibitor. When wells were confluent, single-cell colonies were transferred to a 24-well plate and grown until confluent. Cells were then dissociated and a small amount of cell suspension was harvested in ultrapure water for DNA sequencing before freezing the rest. Positive clones were expanded and the PG-TO-hNGN2 plasmid was integrated into the genome as described above.

Differentiation of iPSCs to day 8 neurons

Differentiation was performed as described previously [103] with minor adjustments. Briefly, iPSCs were cultured as detailed above and upon reaching 70%-80% confluency, cells were transferred to geltrex- or matrigel-coated plates for differentiation. Cells were seeded in induction medium containing DMEM/F12 HEPES (Gibco, 11330032), N2 supplement (Gibco, 17502048), NEAA (Gibco, 11140050) and L-glutamine (Gibco, 25030081), supplemented with ROCK inhibitor (Tocris Bioscience, 1254, 10 μM) and freshly prepared doxycycline (DOX) solution (2 μg/ml, Sigma-Aldrich D9891). Based on plate size, either 1.5 million or 2.5 million iPSCs were seeded in a 10 or 15 cm dish respectively. Induction medium was replaced daily with induction medium containing DOX for three days. On day 2, plates were coated with PDL (Sigma-Aldrich P7405, 0.04mg/ml) overnight. On day 3, plates were washed twice with ultrapure water and dried completely before seeding day 3 neurons per well in maturation medium containing BrainPhys (STEMCELL Technologies, 05790), B27 supplement (Gibco, 17504044), BDNF (PeproTech, 450-02), NT3 (PeproTech, 450-03), Laminin (Gibco, 23017-015) and 40mM BrdU (Sigma-Aldrich, B9285). Neurons were matured with half-medium replacements without BrdU every 2-3 days.

RNA-seq and splicing analysis

RNA was extracted using the miRNeasy Kit (Qiagen) according to the manufacturer's protocol before measuring RNA concentration with a Nanodrop spectrophotometer. RNA-seq libraries were prepared at the Crown Genomics institute of the Nancy and Stephen Grand Israel National Center for Personalized Medicine, Weizmann Institute of Science. Libraries were prepared using the TruSeq Stranded mRNA-seq kit (Illumina) according to the manufacturing protocol. Briefly, the polyA fraction (mRNA) was purified from 500 ng of total input RNA followed by fragmentation and the generation of double-stranded cDNA. After Agencourt Ampure XP beads cleanup (Beckman Coulter), A base addition, adapter ligation and PCR amplification steps were performed. Libraries were quantified by Qubit (Thermo fisher scientific) and TapeStation (Agilent). Sequencing was done on Novaseq 6000 S1 300 cycles kit or Novaseq X 1.5B 300 cycles kit, allocating ~50-60M reads per sample (Illumina; paired end sequencing). In the case of TDP-43^{deltaNLS} and NES samples, sequencing was done with NextSeq high output kit, 75 cycles, allocating ~20M reads per sample (Illumina; single-end sequencing).

Poly-A/T stretches and Illumina adapters were trimmed from RNA sequencing reads using cutadapt [148]; resulting reads shorter than 30bp were discarded. Reads - both those experimentally generated and those from published datasets [17,26,63] - were mapped to the H. sapiens reference genome GRCh38 using STAR [149], supplied with gene annotations downloaded from Ensembl (and with EndToEnd option and outFilterMismatchNoverLmax was set to 0.04). Reads with the same UMI were removed using the PICARD MarkDuplicate tool using the BARCODE_TAG parameter. Pipeline was run using snakemake [150].

Aligned BAMs were used as input for differential splicing analysis with MAJIQ (v2.5.7) [50] using reference genome GRCh38. A deltaPSI threshold of 2% and probability changing threshold of 0.9 was used to calculate the probability of splicing changes between groups. The RNAseq of RBP KD lines was done in several batches (each time including the control line), so for visualization of APP splice events in **Figure 5D**, MAJIQ PSI values were normalized against the corresponding control. For analysis of ROSMAP data, the MAJIQ heterogen function was used to compare between groups and a P-value threshold of 0.05 was maintained. The voila tsv output tables were parsed using an adjusted version of the R script from [17] (see Code Availability) to obtain values per junction instead of per junction cluster. P-values of deltaPSI analyses were calculated as *1 - probability changing*.

Cellular fractionation

Monoclonal iPSC lines carrying APEX constructs mentioned above were differentiated into cortical neurons as described previously. After 5 days of maturation, construct expression was induced for 24 and 4 hours respectively to achieve comparable levels of expression. Cells were washed with PBS once before scraping in lysis buffer A (10 mM Tris Cl, pH 7.5; 10 mM NaCl; 3 mM MgCl2; 0.5% NP40) supplemented with cOmplete Protease Inhibitor Cocktail (Roche, 4693116001) and PhosSTOP (Roche, 4906837001). Lysates were incubated on ice for 10 min while vortexing every few minutes, followed by centrifugation for 10 min at 4°C at maximum speed to precipitate nuclei. After transferring the supernatant (the cytoplasmic fraction) to a new tube, nuclei pellets were repeatedly washed with lysis buffer A via centrifugation for 10 min at 4°C at maximum speed until resuspension was impossible. RIPA buffer (150 mM NaCl; 1% NP40; 0.5% deoxycholate (DOC); 0.1% SDS and 50 mM Tris, pH 8) was added to nuclei pellets before sonication for 3 cycles x 10 sec with 20 sec intervals, using 30-40% power. Samples were centrifuged for 10 min at 4°C at maximum speed to gain nuclear fractions (the supernatant).

APEX proximity labeling

Selected iPSC clones carrying APEX constructs were differentiated into cortical neurons as described above. Construct expression was induced with doxycycline (2 µg/ml, Sigma-Aldrich, D9891) after 5 days of maturation for 24 and 4 hours for TDP-43^{deltaNLS} and NES respectively, to gain comparable expression levels. Samples were then left untreated or incubated with sodium arsenite (250 uM, 90 min, Sigma-Aldrich, S7400) to induce TDP-43 condensate formation. At the same time, biotin-phenol (BP, 500 µM, Iris Biotech GmbH, LS-3500) was supplemented to the media except in the case of negative control samples. In the last minute, APEX activity was induced using H_2O_2 (1 mM, J.T.Baker, 7722-84-1) before halting the labeling with quenching solution (QS: sodium azide (10mM, Mallinckrodt, 1953-57), sodium ascorbate (10mM, Sigma-Aldrich, A7631) and Trolox (5mM, Sigma-Aldrich, 238813) in PBS. Cells were then scraped directly in RIPA lysis buffer (150 mM NaCl, 1% NP40, 0.5% Deoxycholate, 0.1% SDS and 50 mM Tris pH 8 in ultrapure water) containing cOmplete Protease Inhibitor Cocktail (Roche, 4693116001) and PhosSTOP (Roche, 4906837001). Resulting lysates were transferred to microcentrifuge tubes and centrifuged at 15,000 × g for 10 min at 4°C. The supernatant containing proteins was taken to a new tube for quantification of protein concentration with Bio-Rad Protein Assay Dye Reagent (Bio-Rad, 500-0006). Protein samples were brought to the same concentration and incubated on streptavidin-coated magnetic beads (Pierce Streptavidin Magnetic Beads, Thermo-Fisher, 88816) overnight at 4°C with rotation, at a ratio of 100 µl beads per 0.5 mg of sample. The next day, bead samples were washed with a series of

buffers, 1 ml per wash, for 3 minutes at 1100 rpm at room temp to remove non-specific binders: twice with RIPA lysis buffer, once with 1 M KCl (Sigma-Aldrich), once with 0.1 M Na2CO3 (Sigma-Aldrich), and once with 2 M urea in 10 mM Tris-HCl, pH 8.0.

Sample preparation for mass spectrometry

All chemicals are from Sigma-Aldrich Aldrich, unless stated otherwise. Samples were subjected to on-bead tryptic digestion followed by a desalting step. Briefly, washed beads after pull-down were suspended in 8M urea, 0.1M Tris HCl buffer, pH 7.6, and incubated at room temp for 30 min. Proteins were then reduced with 100 mM DTT (5mM final conc) at room temp for 1 hr and then alkylated using iodoacetamide (10 mM final concentration) for 45 min in the dark at room temp. Urea concentration was diluted 5-fold by addition of 50mM ammonium bicarbonate. 250 ng trypsin was then added and samples were incubated at 37°C overnight, followed by a second trypsin digestion (250 ng) for 4 hours at 37°C. Digested peptides were then collected by centrifugation of the beads and transferring the supernatant into a clean tube. Peptides were acidified with trifluoroacetic acid, desalted using HBL Oasis (Waters 094225), speed vac to dryness and stored in -80°C until analysis.

Liquid chromatography and mass spectrometry

Digested proteins were loaded and analyzed using split-less nano-Ultra Performance Liquid Chromatography (10 kpsi nanoAcquity; Waters, Milford, MA, USA). The mobile phase was: A) H_2O + 0.1% formic acid and B) acetonitrile + 0.1% formic acid. Desalting of the samples was performed online using a Symmetry C18 reversed-phase trapping column (180 µm internal diameter, 20 mm length, 5 µm particle size; Waters). The peptides were then separated using a T3 HSS nano-column (75 µm internal diameter, 250 mm length, 1.8 µm particle size; Waters) at 0.35 µL/min. Peptides were eluted from the column into the mass spectrometer using the following gradient: 4% to 26%B in 155 min, 26% to 90%B in 5 min, maintained at 90%B for 5 min and then back to initial conditions. The nanoUPLC was coupled online through a nanoESI emitter (10 µm tip; New Objective; Woburn, MA, USA) to a quadrupole orbitrap mass spectrometer (Q Exactive Plus, Thermo Scientific) using a FlexIon nanospray apparatus (Proxeon). Data was acquired in data dependent acquisition (DDA) mode, using a Top10 method. MS1 resolution was set to 70,000 (at 200m/z) and maximum injection time was set to 60 msec. MS2 resolution was set to 15,000 (at 200m/z) and maximum injection time of 60 msec.

Raw proteomic data analysis

Raw data was analyzed using MaxQuant (v1.6.6.0) [151]. The raw data was searched against the human protein database downloaded from UniprotKB appended with 125 common laboratory contaminant proteins. Enzyme specificity was set to trypsin and up to two missed cleavages were allowed. Fixed modification was set to carbamidomethylation of cysteines and variable modifications were set to oxidation of methionines, asparagine and glutamine deamidation, and protein N-terminal acetylation. Peptide precursor ions were searched with a maximum mass deviation of 4.5 ppm and fragment ions with a maximum mass deviation of 20 ppm. Peptide, protein and site identifications were filtered at an FDR of 1% using the decoy database strategy. The minimal peptide length was 7 amino-acids and the minimum Andromeda score for modified peptides was 40. Peptide identifications were propagated across samples using the match-between-runs option checked. Searches were performed with the label-free quantification option selected.

Proteomics statistical analysis

MaxQuant output table ProteinGroups was imported to Perseus and analyzed as follows. Reverse proteins, proteins identified only based on a modified peptide and contaminants were excluded before log2-transforming the data. Rows were filtered to keep only those with at least 6 valid values, and missing values were replaced by low values from a normal distribution. Two-sample t-test comparing samples with biotin to samples without biotin was performed to remove non-specific binders (FDR < 0.05, log2FC > 0). Samples were separated based on stress condition before filtering to remain only those proteins with a minimum of 2 valid values in at least one experimental group (TDP-43^{deltaNLS} or NES). Missing values were imputed again using a normal distribution. Two-sample t-test using log2-transformed LFQ values was performed to gain proteins enriched in TDP-43^{deltaNLS}.

RNA Extraction and cDNA Synthesis

RNA was extracted from day 8 differentiated cells using the miRNeasy MicroKit (Qiagen) according to the manufacturer's protocol. The RNA concentration was measured using a Nanodrop spectrophotometer, and 500 ng of RNA was used for reverse transcription. First-strand cDNA synthesis was performed using the High-Capacity cDNA Reverse Transcription Kit (Thermo, catalog number 4368814) in accordance with the respective manufacturer's instructions.

RT-PCR

PCR amplification was carried out using the RedTaq Ready Mix PCR Reaction Mix (Sigma-Aldrich, catalog number R2523), which contains RedTaq DNA polymerase, dNTPs, buffer, and magnesium chloride in a pre-mixed, ready-to-use format. The PCR reaction was prepared by combining the following components: 1X final concentration of RedTaq Ready Mix, gene-specific forward and reverse primers, cDNA template, and nuclease-free water to a final reaction volume. For amplification of APP770 specifically, the following primers were used: CCCATTCTTTTACGGCGGATG and AACAGGATCTCGGGCAAGAGG. To amplify the region between exons 6 and 9, primers TCTGTGGAAGAGGTGGTTCG and GGCCTCAAGCCTCTCTTTGG were used. PCR amplification was performed under the following conditions: initial denaturation at 95°C for 5 minutes, followed by 28 cycles of denaturation at 95°C for 30 seconds, primer-specific annealing at the appropriate temperature for 30 seconds, and extension at 72°C for 1 minute. A final extension step was performed at 72°C for 5 minutes. Following amplification, PCR products were analyzed by agarose gel electrophoresis using a 1.8% agarose gel. The PCR products were loaded onto the gel, and electrophoresis was carried out at 120V for approximately 1 hour. The bands were visualized under UV light to confirm the presence and size of the amplified products.

Immunofluorescence and imaging

Differentiation of iPSCs into cortical neurons was done as described above; on day 3, approximately 60,000 neurons were seeded per well of a 96-well plate (Brooks, MGB096-1-2-LG-L). Neurons were fixed on day 8 in 4% PFA in 1X PBS++ for approximately 15 minutes. After one wash with PBS, cells were incubated in 0.1% TritonX in PBS for permeabilization for 10-15 minutes followed by blocking with CasBlock reagent for 10 minutes at room temperature (RT). Primary antibodies (purified anti-β-Amyloid 1-16 Antibody, BioLegend 803004; Thioflavine S, Sigma-Aldrich T1892) were diluted in CasBlock and 75 µl of this mix was added to each well for overnight incubation at 4°C. The next day, cells were washed in PBS twice for 5 minutes. Anti-mouse Cy5 secondary antibody (Jackson ImmunoResearch 715-175-150) was diluted in PBS before incubation with 75 µl per well for 1 hour at RT in the dark. For DNA staining, Hoechst (ThermoFisher 62249, diluted 1:8000 in PBS) was added to the cells after one PBS wash for 10-30 minutes at RT. The Hoechst solution was replaced with PBS before proceeding with imaging. Confocal images were acquired on the Opera Phenix Plus High-Content Imaging System.

Image quantification

A specific CellProfiler (version 4.2.1) [152,153] pipeline was built for quantification of beta-amyloid and thioflavin intensity. First, nuclei were detected with IdentifyPrimaryObject and used as input for Secondary Object identification using the Thioflavine S signal, which was distributed throughout the entire cell. The cytoplasm was demarcated with IdentifyTertiaryObjects by subtracting the nucleus from the Thioflavine S signal. Amyloid intensity was measured in the cytoplasm and averaged across cells per image before plotting and statistical testing in Prism (version 10).

Quantification of puncta was performed using Harmony (version 5.2). Nuclei were segmented from the Hoechst channel using the "Find Nuclei" building block, with parameters optimized to accurately detect individual nuclei. The cytoplasm was then delineated using the "Find Cytoplasm" building block, which expanded outward from the nuclear boundary by utilizing the Cy3 channel, which detects amyloid precursor protein (APP), to generate a whole-cell mask. Beta-amyloid puncta were identified using the "Find Spots" building block in the respective channels. Spot detection parameters, including spot size range and intensity thresholds, were optimized to capture distinct punctate structures while minimizing background noise. The output data, including total puncta count and the number of cells, were exported from Harmony. The number of puncta was then normalized to the number of cells, providing a puncta-to-cell ratio for each field of view.

Mediation analysis

Mediation analysis was conducted to examine whether APP mediates the relationship between TDP-43 pathology and amyloid-β pathology. When modeling different isoforms of APP into a single ratio variable (e.g., $\frac{APP571+APP770}{1+APP695}$), each APP isoform underwent min-max scaling before computing the sum/ratio. The total, direct, and indirect effects were estimated using Ordinary Least Squares (OLS) regression models (**Table 3**). First, we assessed the effect of TDP-43 on APP (path a). Next, we examined the effect of APP on amyloid-β while controlling for TDP-43 (path b). The total effect (c) of TDP-43 on amyloid-β was decomposed into the direct effect (c', TDP-43's effect on amyloid-β independent of APP) and the indirect effect ($a \times b$), representing mediation. To test the statistical significance of the indirect effect, we used bias-corrected bootstrap confidence intervals (95% CI) with n = 1,000 resamples. The proportion of the total effect mediated was computed as $\frac{(a \times b)}{c}$. All statistical analyses were performed in Python 3.6 using the statsmodels package, and results were considered statistically significant at $p < 0.05$.

Acknowledgements

We wish to thank Michael Ward (NINDS, NIH) and Bill Skarnes (Jackson labs) for access to iPSC lines. We thank Alon Savidor (WIS) and Yishai Levin (WIS) for mass spectrometry, and Inbal Bolocan Nachman (WIS) and Yuval Elazari (WIS) for RNA sequencing. We also thank Noa Wigoda (WIS), Melina Klostermann (Julius-Maximilians-Universität Würzburg) and the BioCiphers team for bioinformatics advice. To Prof. Naomi Habib and Anael Cain (HUJI) we are grateful for advice and discussions. We thank Anna-Leigh Brown (UCL), Jack Humphrey (MSSM) and Pietro Fratta (UCL) for advice on splicing.

EH is the Mondry Family Professorial Chair and Head of the Andrea L. and Lawrence A. Wolfe Family Center for Research on Neuroimmunology and Neuromodulation. Funding for research: Binational Science Foundation (BSF); Association Francaise Contre les Myopathies (AFM); Amyotrophic Lateral Sclerosis Association (ALSA); Target ALS; Israel Science Foundation (ISF 3497/21, 424/22, 494/24); ALS Canada; Minna-James-Heineman Stiftung through Minerva, Minerva Foundation, with funding from the Federal German Ministry for Education and Research; Robert Packard Center for ALS Research at Johns Hopkins; McGill University; EU - ERA-Net; Radala Foundation for ALS Research; Additional support generously provided by the Kekst Family Institute for Medical Genetics. Weizmann SABRA - Yeda-Sela - WRC Program, the Estate of Emile Mimran, and The Maurice and Vivienne Wohl Biology Endowment. Nella and Leon Benoziyo Center for Neurological Diseases. Goldhirsh-Yellin Foundation. Dr. Sydney Brenner and friends. Weizmann - Center for Research on Neurodegeneration. Redhill Foundation – Sam and Jean Rothberg Charitable Trust Dr. Dvora and Haim Teitelbaum Endowment Fund. LM is funded by a Minerva Postdoctoral Fellowship. YDM is funded by the Weizmann - CNRS (Centre National de la Recherche Scientifique) Collaboration Program.

ROSMAP is supported by P30AG10161, P30AG72975, R01AG15819, R01AG17917, U01AG46152, and U01AG61356. ROSMAP resources can be requested at https://www.radc.rush.edu and www.synpase.org.

References

1. Birsa, N., Bentham, M. P. & Fratta, P. Cytoplasmic functions of TDP-43 and FUS and their role in ALS. *Seminars in Cell and Developmental Biology* vol. 99 193–201 Preprint at https://doi.org/10.1016/j.semcdb.2019.05.023 (3 2020).
2. Ratti, A. & Buratti, E. Physiological functions and pathobiology of TDP-43 and FUS/TLS proteins. *Journal of Neurochemistry* vol. 138 Suppl 95–111 Preprint at https://doi.org/10.1111/jnc.13625 (8 2016).
3. Neumann, M. *et al.* Ubiquitinated TDP-43 in frontotemporal lobar degeneration and amyotrophic lateral sclerosis. *Science* **314**, 130–133 (10 2006).
4. Suk, T. R. & Rousseaux, M. W. C. The role of TDP-43 mislocalization in amyotrophic lateral sclerosis. *Mol. Neurodegener.* **15**, (8 2020).
5. Arai, T. *et al.* Phosphorylated TDP-43 in Alzheimer's disease and dementia with Lewy bodies. *Acta Neuropathol.* **117**, 125–136 (2009).
6. Meneses, A. *et al.* TDP-43 Pathology in Alzheimer's Disease. *Mol. Neurodegener.* **16**, (12 2021).
7. Tomé, S. O. *et al.* TDP-43 pathology is associated with increased tau burdens and seeding. *Mol. Neurodegener.* **18**, 71 (2023).
8. Davis, S. A., Gan, K. A., Dowell, J. A., Cairns, N. J. & Gitcho, M. A. TDP-43 expression influences amyloidβ plaque deposition and tau aggregation. *Neurobiol. Dis.* **103**, 154–162 (2017).
9. Shih, Y.-H. *et al.* TDP-43 interacts with amyloid-β, inhibits fibrillization, and worsens pathology in a model of Alzheimer's disease. *Nat. Commun.* **11**, 5950 (2020).
10. Nikom, D. & Zheng, S. Alternative splicing in neurodegenerative disease and the promise of RNA therapies. *Nat. Rev. Neurosci.* **24**, 457–473 (2023).
11. Sattler, R. & Donnelly, C. J. *RNA Metabolism in Neurodegenerative Diseases*. (Springer, 2018).
12. Jeong, Y. H. *et al.* Tdp-43 cryptic exons are highly variable between cell types. *Mol Neurodegener* **12**,

13 (2017).

13. Sun, M. *et al.* Cryptic exon incorporation occurs in Alzheimer's brain lacking TDP-43 inclusion but exhibiting nuclear clearance of TDP-43. *Acta Neuropathol.* **133**, 923–931 (2017).
14. Humphrey, J., Emmett, W., Fratta, P., Isaacs, A. M. & Plagnol, V. Quantitative analysis of cryptic splicing associated with TDP-43 depletion. *BMC Med Genomics* **10**, 38 (2017).
15. Seddighi, S. *et al.* Mis-spliced transcripts generate de novo proteins in TDP-43-related ALS/FTD. *Sci. Transl. Med.* (1 2024) doi:10.1126/SCITRANSLMED.ADG7162.
16. Ma, X. R. *et al.* TDP-43 represses cryptic exon inclusion in the FTD-ALS gene UNC13A. *Nature* **603**, 124–130 (2022).
17. Brown, A.-L. *et al.* TDP-43 loss and ALS-risk SNPs drive mis-splicing and depletion of UNC13A. *Nature* **603**, 131–137 (2022).
18. Klim, J. R. *et al.* ALS-implicated protein TDP-43 sustains levels of STMN2, a mediator of motor neuron growth and repair. *Nat. Neurosci.* **22**, 167–179 (2019).
19. Ling, J. P., Pletnikova, O., Troncoso, J. C. & Wong, P. C. TDP-43 repression of nonconserved cryptic exons is compromised in ALS-FTD. *Science* **349**, 650–655 (2015).
20. Melamed, Z. 'ev *et al.* Premature polyadenylation-mediated loss of stathmin-2 is a hallmark of TDP-43-dependent neurodegeneration. *Nat. Neurosci.* **22**, 180–190 (2019).
21. Prudencio, M. *et al.* Truncated stathmin-2 is a marker of TDP-43 pathology in frontotemporal dementia. *J. Clin. Invest.* **130**, 6080–6092 (2020).
22. Agra Almeida Quadros, A. R. *et al.* Cryptic splicing of stathmin-2 and UNC13A mRNAs is a pathological hallmark of TDP-43-associated Alzheimer's disease. *Acta Neuropathol.* **147**, 9 (2024).
23. Nguyen, T. B. *et al.* Aberrant splicing in Huntington's disease accompanies disrupted TDP-43 activity and altered m6A RNA modification. *Nat Neurosci* **28**, 280–292 (2025).
24. Estades Ayuso, V. *et al.* TDP-43-regulated cryptic RNAs accumulate in Alzheimer's disease brains.

Mol Neurodegener **18**, 57 (2023).

25. Tollervey, J. R. *et al.* Characterizing the RNA targets and position-dependent splicing regulation by TDP-43. *Nat. Neurosci.* **14**, 452–458 (4 2011).
26. Liu, E. Y. *et al.* Loss of Nuclear TDP-43 Is Associated with Decondensation of LINE Retrotransposons. *Cell Rep.* **27**, 1409–1421.e6 (2019).
27. Raj, T. *et al.* Integrative transcriptome analyses of the aging brain implicate altered splicing in Alzheimer's disease susceptibility. *Nat. Genet.* **50**, 1584–1592 (11 2018).
28. Kim, S., Han, S., Nho, K., Lee, Y. & Koh, I. Brain regional alternative splicing and clinical traits in Alzheimer's disease. *Alzheimers. Dement.* **19**, e068340 (2023).
29. Love, J. E., Hayden, E. J. & Rohn, T. T. Alternative splicing in Alzheimer's disease. *J. Parkinsons Dis. Alzheimers Dis.* **2**, 6 (2015).
30. Adusumalli, S., Ngian, Z.-K., Lin, W.-Q., Benoukraf, T. & Ong, C.-T. Increased intron retention is a post-transcriptional signature associated with progressive aging and Alzheimer's disease. *Aging Cell* **18**, e12928 (2019).
31. Braggin, J. E. *et al.* Alternative splicing in a presenilin 2 variant associated with Alzheimer disease. *Ann. Clin. Transl. Neurol.* **6**, 762–777 (2019).
32. Han, S. *et al.* Identification of exon skipping events associated with Alzheimer's disease in the human hippocampus. *BMC Med. Genomics* **12**, 13 (2019).
33. Lee, Y. *et al.* Genetic variation affecting exon skipping contributes to brain structural atrophy in Alzheimer's disease. *AMIA Summits Transl. Sci. Proc.* **2017**, 124–131 (2018).
34. O'Brien, R. J. & Wong, P. C. Amyloid precursor protein processing and Alzheimer's disease. *Annual review of neuroscience* vol. 34 185–204 Preprint at https://doi.org/10.1146/ANNUREV-NEURO-061010-113613 (7 2011).
35. Orobets, K. S. & Karamyshev, A. L. Amyloid precursor protein and Alzheimer's disease. *Int. J. Mol.*

Sci. **24**, (2023).

36. Yang, L.-B. *et al.* Elevated beta-secretase expression and enzymatic activity detected in sporadic Alzheimer disease. *Nat. Med.* **9**, 3–4 (2003).
37. Johnston, J. A. *et al.* Expression and activity of beta-site amyloid precursor protein cleaving enzyme in Alzheimer's disease. *Biochem. Soc. Trans.* **33**, 1096–1100 (2005).
38. Lanoiselée, H.-M. *et al.* APP, PSEN1, and PSEN2 mutations in early-onset Alzheimer disease: A genetic screening study of familial and sporadic cases. *PLoS Med.* **14**, e1002270 (2017).
39. Andrade-Guerrero, J. *et al.* Alzheimer's disease: An updated overview of its genetics. *Int. J. Mol. Sci.* **24**, 3754 (2023).
40. Weggen, S. & Beher, D. Molecular consequences of amyloid precursor protein and presenilin mutations causing autosomal-dominant Alzheimer's disease. *Alzheimers. Res. Ther.* **4**, 9 (2012).
41. Nalivaeva, N. N. & Turner, A. J. The amyloid precursor protein: a biochemical enigma in brain development, function and disease. *FEBS Lett.* **587**, 2046–2054 (6 2013).
42. Sandbrink, R., Masters, C. L. & Beyreuther, K. APP gene family. Alternative splicing generates functionally related isoforms. *Ann. N. Y. Acad. Sci.* **777**, 281–287 (1996).
43. Moir, R. D. *et al.* Relative increase in Alzheimer's disease of soluble forms of cerebral Abeta amyloid protein precursor containing the Kunitz protease inhibitory domain. *J. Biol. Chem.* **273**, 5013–5019 (2 1998).
44. Urakami, K. *et al.* Amyloid beta protein precursors with kunitz-type inhibitor domains and acetylcholinesterase in cerebrospinal fluid from patients with dementia of the Alzheimer type. *Acta Neurol. Scand.* **85**, 343–346 (1992).
45. Bordji, K., Becerril-Ortega, J., Nicole, O. & Buisson, A. Activation of extrasynaptic, but not synaptic, NMDA receptors modifies amyloid precursor protein expression pattern and increases amyloid-ß production. *J. Neurosci.* **30**, 15927–15942 (2010).

46. Tanaka, S. *et al.* Three types of amyloid protein precursor mRNA in human brain: their differential expression in Alzheimer's disease. *Biochem. Biophys. Res. Commun.* **157**, 472–479 (1988).

47. Zhan, S. S., Sandbrink, R., Beyreuther, K. & Schmitt, H. P. APP with Kunitz type protease inhibitor domain (KPI) correlates with neuritic plaque density but not with cortical synaptophysin immunoreactivity in Alzheimer's disease and non-demented aged subjects: a multifactorial analysis. *Clin. Neuropathol.* **14**, 142–149 (1995).

48. Bennett, D. A. *et al.* Religious Orders Study and Rush Memory and Aging Project. *J. Alzheimers. Dis.* **64**, S161–S189 (2018).

49. Logsdon, B. ROSMAP RNAseq BAM files. Synapse https://doi.org/10.7303/SYN4164376 (2016).

50. Vaquero-Garcia, J. *et al.* A new view of transcriptome complexity and regulation through the lens of local splicing variations. *eLife* vol. 5 Preprint at https://doi.org/10.7554/ELIFE.11752 (2 2016).

51. Zeng, F.-F. *et al.* Association of PICALM gene polymorphisms with Alzheimer's disease: Evidence from an updated meta-analysis. *Curr. Alzheimer Res.* **16**, 1196–1205 (2019).

52. Chen, K., Gao, T., Bai, Z. & Yuan, Z. Circulating APP, NCAM and Aβ serve as biomarkers for Alzheimer's disease. *Brain Res.* **1699**, 117–120 (2018).

53. Aisa, B. *et al.* Altered NCAM expression associated with the cholinergic system in Alzheimer's disease. *J. Alzheimers. Dis.* **20**, 659–668 (2010).

54. Gamir-Morralla, A. *et al.* Kidins220 correlates with tau in Alzheimer's disease brain and cerebrospinal fluid. *J. Alzheimers. Dis.* **55**, 1327–1333 (2017).

55. Buchholz, S. & Zempel, H. The six brain-specific TAU isoforms and their role in Alzheimer's disease and related neurodegenerative dementia syndromes. *Alzheimers. Dement.* **20**, 3606–3628 (2024).

56. Oltersdorf, T. *et al.* The secreted form of the Alzheimer's amyloid precursor protein with the Kunitz domain is protease nexin-II. *Nature* **341**, 144–147 (1989).

57. Kitaguchi, N., Takahashi, Y., Tokushima, Y., Shiojiri, S. & Ito, H. Novel precursor of Alzheimer's disease

amyloid protein shows protease inhibitory activity. *Nature* **331**, 530–532 (1988).

58. Li, B. & Dewey, C. N. RSEM: accurate transcript quantification from RNA-Seq data with or without a reference genome. *BMC Bioinformatics* **12**, 323 (8 2011).
59. Bionetworks, S. Gene Expression (RNA seq - bulk brain). https://www.synapse.org/Synapse:syn3388564/version/.
60. Kapasi, A. *et al.* High-throughput digital quantification of Alzheimer disease pathology and associated infrastructure in large autopsy studies. *J. Neuropathol. Exp. Neurol.* **82**, 976–986 (2023).
61. Variable Details. https://www.radc.rush.edu/docs/var/detail.htm?category=Pathology&subcategory=Beta-Amyloid&variable=amylsqrt_est_8reg.
62. Seifar, F. *et al.* Large-scale deep proteomic analysis in Alzheimer's disease brain regions across race and ethnicity. *Alzheimers. Dement.* **20**, 8878–8897 (2024).
63. Roczniak-Ferguson, A. & Ferguson, S. M. Pleiotropic requirements for human TDP-43 in the regulation of cell and organelle homeostasis. *Life Sci. Alliance* **2**, e201900358 (2019).
64. Krispin, S. *et al.* Organellomics: AI-driven deep organellar phenotyping reveals novel ALS mechanisms in human neurons. (2024) doi:10.1101/2024.01.31.572110.
65. Ashburner, M. *et al.* Gene Ontology: tool for the unification of biology. *Nature Genetics 2000 25:1* **25**, 25–29 (5 2000).
66. Consortium, T. G. O. *et al.* The Gene Ontology knowledgebase in 2023. *Genetics* **224**, (5 2023).
67. David, G. *et al.* The RNA-binding proteins CELF1 and ELAVL1 cooperatively control the alternative splicing of CD44. *Biochem. Biophys. Res. Commun.* **626**, 79–84 (2022).
68. Xia, H. *et al.* CELF1 preferentially binds to exon-intron boundary and regulates alternative splicing in HeLa cells. *Biochim. Biophys. Acta* **1860**, 911–921 (2017).
69. Xiao, J., Jin, S., Wang, X., Huang, J. & Zou, H. CELF1 selectively regulates Alternative Splicing of DNA

repair genes associated with cataract in human lens cell line. *Biochem. Genet.* **61**, 1319–1333 (2023).

70. Millevoi, S. *et al.* An interaction between U2AF 65 and CF I(m) links the splicing and 3' end processing machineries. *EMBO J.* **25**, 4854–4864 (2006).
71. Bai, R. *et al.* Structure of the activated human minor spliceosome. *Science* **371**, eabg0879 (2021).
72. Dardenne, E. *et al.* RNA helicases DDX5 and DDX17 dynamically orchestrate transcription, miRNA, and splicing programs in cell differentiation. *Cell Rep.* **7**, 1900–1913 (2014).
73. He, C., Zhang, G., Lu, Y., Zhou, J. & Ren, Z. DDX17 modulates the expression and alternative splicing of genes involved in apoptosis and proliferation in lung adenocarcinoma cells. *PeerJ* **10**, e13895 (2022).
74. Taylor, K. *et al.* Modulatory role of RNA helicases in MBNL-dependent alternative splicing regulation. *Cell. Mol. Life Sci.* **80**, 335 (2023).
75. Gencheva, M., Kato, M., Newo, A. N. S. & Lin, R.-J. Contribution of DEAH-box protein DHX16 in human pre-mRNA splicing. *Biochem. J.* **429**, 25–32 (2010).
76. Weng, M.-T. & Luo, J. The enigmatic ERH protein: its role in cell cycle, RNA splicing and cancer. *Protein Cell* **4**, 807–812 (2013).
77. Kozlowski, P. Thirty years with ERH: An mRNA splicing and mitosis factor only or rather a novel genome integrity protector? *Cells* **12**, 2449 (2023).
78. Kroupova, A. *et al.* Molecular architecture of the human tRNA ligase complex. *Elife* **10**, (2021).
79. Oberdoerffer, S. *et al.* Regulation of CD45 alternative splicing by heterogeneous ribonucleoprotein, hnRNPLL. *Science* **321**, 686–691 (2008).
80. Chang, X., Li, B. & Rao, A. RNA-binding protein hnRNPLL regulates mRNA splicing and stability during B-cell to plasma-cell differentiation. *Proc. Natl. Acad. Sci. U. S. A.* **112**, E1888–97 (2015).
81. Wang, X. *et al.* hnRNPLL controls pluripotency exit of embryonic stem cells by modulating

alternative splicing of Tbx3 and Bptf. *EMBO J.* **40**, e104729 (2 2021).

82. Chen, X. *et al.* hnRNPLL regulates MYOF alternative splicing and correlates with early metastasis in pancreatic ductal adenocarcinoma. *Cancer Lett.* **611**, 217436 (2024).
83. Dagher, S. F., Wang, J. L. & Patterson, R. J. Identification of galectin-3 as a factor in pre-mRNA splicing. *Proc. Natl. Acad. Sci. U. S. A.* **92**, 1213–1217 (1995).
84. Voss, P. G., Haudek, K. C., Patterson, R. J. & Wang, J. L. Galectin-3-U1 snRNP complexes initiate splicing activity in U1-depleted nuclear extracts. *Methods Mol. Biol.* **2442**, 713–726 (2022).
85. Straub, T. *et al.* The RNA-splicing factor PSF/p54 controls DNA-topoisomerase I activity by a direct interaction. *J. Biol. Chem.* **273**, 26261–26264 (1998).
86. Fox, A. H. & Lamond, A. I. Paraspeckles. *Cold Spring Harb. Perspect. Biol.* **2**, a000687 (2010).
87. Vuong, J. K. *et al.* PTBP1 and PTBP2 serve both specific and redundant functions in neuronal pre-mRNA splicing. *Cell Rep.* **17**, 2766–2775 (2016).
88. Rossi, F. *et al.* Involvement of U1 small nuclear ribonucleoproteins (snRNP) in 5’ splice site-U1 snRNP interaction. *J. Biol. Chem.* **271**, 23985–23991 (1996).
89. Heinrichs, V., Bach, M., Winkelmann, G. & Lührmann, R. U1-specific protein C needed for efficient complex formation of U1 snRNP with a 5’ splice site. *Science* **247**, 69–72 (1990).
90. Ge, H., Zuo, P. & Manley, J. L. Primary structure of the human splicing factor ASF reveals similarities with Drosophila regulators. *Cell* **66**, 373–382 (1991).
91. Das, S. & Krainer, A. R. Emerging functions of SRSF1, splicing factor and oncoprotein, in RNA metabolism and cancer. *Mol. Cancer Res.* **12**, 1195–1204 (2014).
92. Zahler, A. M., Lane, W. S., Stolk, J. A. & Roth, M. B. SR proteins: a conserved family of pre-mRNA splicing factors. *Genes Dev.* **6**, 837–847 (1992).
93. Long, J. C. & Caceres, J. F. The SR protein family of splicing factors: master regulators of gene expression. *Biochem. J.* **417**, 15–27 (2009).

94. Fu, X. D. & Maniatis, T. Isolation of a complementary DNA that encodes the mammalian splicing factor SC35. *Science* **256**, 535–538 (1992).

95. Li, K. & Wang, Z. Splicing factor SRSF2-centric gene regulation. *Int. J. Biol. Sci.* **17**, 1708–1715 (2021).

96. Tan, W., Wang, W. & Ma, Q. Physiological and pathological function of Serine/arginine-rich splicing factor 4 and related diseases. *Biomed Res. Int.* **2018**, 3819719 (2018).

97. Screaton, G. R. *et al.* Identification and characterization of three members of the human SR family of pre-mRNA splicing factors. *EMBO J.* **14**, 4336–4349 (1995).

98. Yang, S., Jia, R. & Bian, Z. SRSF5 functions as a novel oncogenic splicing factor and is upregulated by oncogene SRSF3 in oral squamous cell carcinoma. *Biochim. Biophys. Acta Mol. Cell Res.* **1865**, 1161–1172 (2018).

99. She, W., Shao, J. & Jia, R. Targeting splicing factor SRSF6 for cancer therapy. *Front. Cell Dev. Biol.* **9**, 780023 (2021).

100. Yoh, S. M., Cho, H., Pickle, L., Evans, R. M. & Jones, K. A. The Spt6 SH2 domain binds Ser2-P RNAPII to direct Iws1-dependent mRNA splicing and export. *Genes Dev.* **21**, 160–174 (2007).

101. Martín, E., Vivori, C., Rogalska, M., Herrero-Vicente, J. & Valcárcel, J. Alternative splicing regulation of cell-cycle genes by SPF45/SR140/CHERP complex controls cell proliferation. *RNA* **27**, 1557–1576 (2021).

102. Deng, L. *et al.* MYC-driven U2SURP regulates alternative splicing of SAT1 to promote triple-negative breast cancer progression. *Cancer Lett.* **560**, 216124 (2023).

103. Fernandopulle, M. S. *et al.* Transcription Factor-Mediated Differentiation of Human iPSCs into Neurons. *Curr. Protoc. Cell Biol.* **79**, e51 (6 2018).

104. Ratti, A. *et al.* Chronic stress induces formation of stress granules and pathological TDP-43 aggregates in human ALS fibroblasts and iPSC-motoneurons. *Neurobiol. Dis.* 105051 (8 2020).

105. Gasset-Rosa, F. *et al.* Cytoplasmic TDP-43 De-mixing Independent of Stress Granules Drives

Inhibition of Nuclear Import, Loss of Nuclear TDP-43, and Cell Death. *Neuron* vol. 102 339–357.e7 Preprint at (4 2019).

106. Smeltzer, S. *et al.* Hypusination of Eif5a regulates cytoplasmic TDP-43 aggregation and accumulation in a stress-induced cellular model. *Biochim. Biophys. Acta Mol. Basis Dis.* **1867**, 165939 (2021).
107. Higashi, S. *et al.* TDP-43 associates with stalled ribosomes and contributes to cell survival during cellular stress. *J. Neurochem.* **126**, 288–300 (2013).
108. McGurk, L. *et al.* Poly(ADP-Ribose) Prevents Pathological Phase Separation of TDP-43 by Promoting Liquid Demixing and Stress Granule Localization. *Mol. Cell* **71**, 703–717.e9 (9 2018).
109. Colombrita, C. *et al.* TDP-43 is recruited to stress granules in conditions of oxidative insult. *J. Neurochem.* **111**, 1051–1061 (2009).
110. Hans, F., Glasebach, H. & Kahle, P. J. Multiple distinct pathways lead to hyperubiquitylated insoluble TDP-43 protein independent of its translocation into stress granules. *J. Biol. Chem.* **295**, 673–689 (2020).
111. Meyerowitz, J. *et al.* C-Jun N-terminal kinase controls TDP-43 accumulation in stress granules induced by oxidative stress. *Mol. Neurodegener.* **6**, 57 (2011).
112. Cohen, T. J., Lee, V. M. Y. & Trojanowski, J. Q. TDP-43 functions and pathogenic mechanisms implicated in TDP-43 proteinopathies. *Trends in Molecular Medicine* vol. 17 659–667 Preprint at https://doi.org/10.1016/j.molmed.2011.06.004 (11 2011).
113. Dasgupta, T. & Ladd, A. N. The importance of CELF control: molecular and biological roles of the CUG-BP, Elav-like family of RNA-binding proteins. *Wiley Interdiscip. Rev. RNA* **3**, 104–121 (1 2012).
114. Förch, P. *et al.* The Apoptosis-Promoting Factor TIA-1 Is a Regulator of Alternative Pre-mRNA Splicing. *Molecular Cell* vol. 6 1089–1098 Preprint at https://doi.org/10.1016/S1097-2765(00)00107-6 (11 2000).
115. Gatto-Konczak, F. D. *et al.* The RNA-Binding Protein TIA-1 Is a Novel Mammalian Splicing Regulator

Acting through Intron Sequences Adjacent to a 5′ Splice Site. *https://doi. org/10. 1128/MCB. 20. 17. 6287-6299. 2000* vol. 20 6287–6299 Preprint at https://doi.org/10.1128/MCB.20.17.6287-6299.2000 (9 2023).

116. Komor, A. C., Kim, Y. B., Packer, M. S., Zuris, J. A. & Liu, D. R. Programmable editing of a target base in genomic DNA without double-stranded DNA cleavage. *Nature* **533**, 420–424 (4 2016).
117. Mallory, M. J. *et al.* Signal- and development-dependent alternative splicing of LEF1 in T cells is controlled by CELF2. *Mol. Cell. Biol.* **31**, 2184–2195 (2011).
118. Mallory, M. J. *et al.* Induced transcription and stability of CELF2 mRNA drives widespread alternative splicing during T-cell signaling. *Proc. Natl. Acad. Sci. U. S. A.* **112**, E2139–48 (2015).
119. Yanaizu, M., Washizu, C., Nukina, N., Satoh, J.-I. & Kino, Y. CELF2 regulates the species-specific alternative splicing of TREM2. *Sci. Rep.* **10**, 17995 (2020).
120. Lai, S. *et al.* N6-methyladenosine-mediated CELF2 regulates CD44 alternative splicing affecting tumorigenesis via ERAD pathway in pancreatic cancer. *Cell Biosci.* **12**, 125 (2022).
121. Ladd, A. N., Charlet, N. & Cooper, T. A. The CELF family of RNA binding proteins is implicated in cell-specific and developmentally regulated alternative splicing. *Mol. Cell. Biol.* **21**, 1285–1296 (2001).
122. Zhang, W.-J. & Wu, J. Y. Sip1, a novel RS domain-containing protein essential for pre-mRNA splicing. *Mol. Cell. Biol.* **18**, 676–684 (1998).
123. Zhao, W. *et al.* HuR and TIA1/TIAL1 are involved in regulation of alternative splicing of SIRT1 pre-mRNA. *Int. J. Mol. Sci.* **15**, 2946–2958 (2014).
124. Izquierdo, J. M. & Valcárcel, J. Two isoforms of the T-cell intracellular antigen 1 (TIA-1) splicing factor display distinct splicing regulation activities. Control of TIA-1 isoform ratio by TIA-1-related protein: Control of Tia-1 isoform ratio by Tia-1-related protein. *J. Biol. Chem.* **282**, 19410–19417 (2007).
125. Aznarez, I. *et al.* A systematic analysis of intronic sequences downstream of 5’ splice sites reveals a

widespread role for U-rich motifs and TIA1/TIAL1 proteins in alternative splicing regulation. *Genome Res.* **18**, 1247–1258 (2008).

126. Mackenzie, I. R. *et al.* TIA1 Mutations in Amyotrophic Lateral Sclerosis and Frontotemporal Dementia Promote Phase Separation and Alter Stress Granule Dynamics. *Neuron* **95**, 808–816.e9 (8 2017).

127. Hirsch-Reinshagen, V. *et al.* Clinical and neuropathological features of ALS/FTD with TIA1 mutations. *Acta neuropathologica communications* vol. 5 96 Preprint at https://doi.org/10.1186/S40478-017-0493-X/FIGURES/5 (12 2017).

128. Osma-Garcia, I. C. *et al.* The splicing regulators TIA1 and TIAL1 are required for the expression of the DNA damage repair machinery during B cell lymphopoiesis. *Cell reports* vol. 41 Preprint at https://doi.org/10.1016/J.CELREP.2022.111869 (12 2022).

129. Wang, Y., Liu, J. & Zhou, F. The role of TIA1 and TIAL1 in germinal center B cell function and survival. *Cell. Mol. Immunol.* **20**, 1090–1092 (2023).

130. Zhao, W. *et al.* POSTAR3: an updated platform for exploring post-transcriptional regulation coordinated by RNA-binding proteins. *Nucleic Acids Res.* **50**, D287–D294 (1 2022).

131. Riku, Y. *et al.* TDP-43 Proteinopathy and Tauopathy: Do They Have Pathomechanistic Links? *Int. J. Mol. Sci.* **23**, (12 2022).

132. Vogt, M. A. *et al.* TDP-43 induces p53-mediated cell death of cortical progenitors and immature neurons. *Sci. Rep.* **8**, 8097 (2018).

133. Walker, A. K. *et al.* Functional recovery in new mouse models of ALS/FTLD after clearance of pathological cytoplasmic TDP-43. *Acta Neuropathol.* **130**, 643–660 (11 2015).

134. Josephs, K. A. *et al.* TDP-43 is a key player in the clinical features associated with Alzheimer's disease. *Acta Neuropathol.* **127**, 811–824 (2014).

135. Katsumata, Y., Fardo, D. W., Kukull, W. A. & Nelson, P. T. Dichotomous scoring of TDP-43

proteinopathy from specific brain regions in 27 academic research centers: associations with Alzheimer's disease and cerebrovascular disease pathologies. *Acta Neuropathol. Commun.* **6**, 142 (2018).

136. Donev, R., Newall, A., Thome, J. & Sheer, D. A role for SC35 and hnRNPA1 in the determination of amyloid precursor protein isoforms. *Mol. Psychiatry* **12**, 681–690 (2007).

137. Bayram, E., Shan, G. & Cummings, J. L. Associations between comorbid TDP-43, Lewy body pathology, and neuropsychiatric symptoms in Alzheimer's disease. *J. Alzheimers. Dis.* **69**, 953–961 (2019).

138. Wennberg, A. M. *et al.* Association of apolipoprotein E ε4 with transactive response DNA-binding protein 43. *JAMA Neurol.* **75**, 1347–1354 (2018).

139. Finkel, R. S. *et al.* Nusinersen versus sham control in infantile-onset spinal muscular atrophy. *N. Engl. J. Med.* **377**, 1723–1732 (2017).

140. Mercuri, E. *et al.* Nusinersen versus sham control in later-onset spinal muscular atrophy. *N. Engl. J. Med.* **378**, 625–635 (2018).

141. Bennett, C. F., Krainer, A. R. & Cleveland, D. W. Antisense oligonucleotide therapies for neurodegenerative diseases. *Annu. Rev. Neurosci.* **42**, 385–406 (2019).

142. Baughn, M. W. *et al.* Mechanism of STMN2 cryptic splice-polyadenylation and its correction for TDP-43 proteinopathies. *Science* **379**, 1140–1149 (3 2023).

143. Keuss, M. J. *et al.* Loss of TDP-43 induces synaptic dysfunction that is rescued by UNC13A splice-switching ASOs. *bioRxiv* 2024.06.20.599684 (6 2024).

144. Agrawal, S. *et al.* Limbic-predominant age-related TDP-43 encephalopathy neuropathologic change and microvascular pathologies in community-dwelling older persons. *Brain Pathol.* **31**, e12939 (2021).

145. Agrawal, S. *et al.* Hippocampal neuronal loss and cognitive decline in LATE-NC and ADNC among

community-dwelling older persons. *Alzheimers. Dement.* **21**, e14500 (2025).

146. Pantazis, C. B. *et al.* A reference human induced pluripotent stem cell line for large-scale collaborative studies. *Cell Stem Cell* **29**, 1685–1702.e22 (12 2022).

147. Coelho, M. A. *et al.* Base editing screens map mutations affecting interferon-γ signaling in cancer. *Cancer Cell* **41**, 288–303.e6 (2023).

148. Martin, M. Cutadapt removes adapter sequences from high-throughput sequencing reads. *EMBnet j.* **17**, 10 (2011).

149. Dobin, A. *et al.* STAR: ultrafast universal RNA-seq aligner. *Bioinformatics* **29**, 15–21 (2013).

150. Köster, J. & Rahmann, S. Snakemake--a scalable bioinformatics workflow engine. *Bioinformatics* **28**, 2520–2522 (2012).

151. Cox, J. & Mann, M. MaxQuant enables high peptide identification rates, individualized p.p.b.-range mass accuracies and proteome-wide protein quantification. *Nat. Biotechnol.* **26**, 1367–1372 (2008).

152. Carpenter, A. E. *et al.* CellProfiler: image analysis software for identifying and quantifying cell phenotypes. *Genome Biol.* **7**, (10 2006).

153. Stirling, D. R. *et al.* CellProfiler 4: improvements in speed, utility and usability. *BMC Bioinformatics* **22**, (12 2021).

154. Perez-Riverol, Y. *et al.* The PRIDE database at 20 years: 2025 update. *Nucleic Acids Res.* **53**, D543–D553 (2025).